

# Electronic Structure of a Weakly Antiferromagnetically Coupled Mn<sup>II</sup>Mn<sup>III</sup> Model Relevant to Manganese Proteins: A Combined EPR, <sup>55</sup>Mn-ENDOR, and DFT Study

Nicholas Cox,<sup>\*,†</sup> William Ames,<sup>†,‡</sup> Boris Epel,<sup>†</sup> Leonid V. Kulik,<sup>§</sup> Leonid Rapatskiy,<sup>†</sup> Frank Neese,<sup>†,‡</sup> Johannes Messinger,<sup>||</sup> Karl Wieghardt,<sup>†</sup> and Wolfgang Lubitz<sup>\*,†</sup>

<sup>†</sup>Max-Planck-Institut für Bioorganische Chemie, Stiftstrasse 34-36, D-45470 Mülheim an der Ruhr, Germany

<sup>‡</sup>Lehrstuhl für Theoretische Chemie, Institut für Physikalische und Theoretische Chemie, Universität Bonn, Wegelerstrasse 12, D-53115 Bonn, Germany

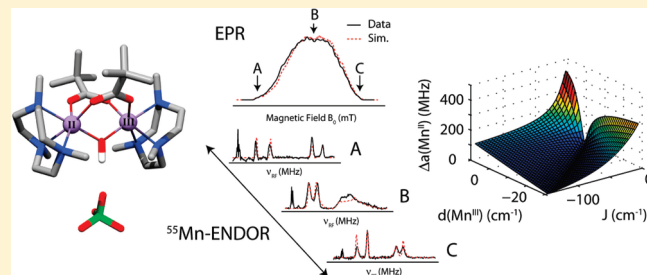
<sup>§</sup>Institute of Chemical Kinetics and Combustion, Institutskaya 3, 630090 Novosibirsk, Russia

<sup>||</sup>Department of Chemistry, Kemiskt Biologiskt Centrum (KBC), Umeå University, S-90187 Umeå, Sweden

## Supporting Information

**ABSTRACT:** An analysis of the electronic structure of the [Mn<sup>II</sup>Mn<sup>III</sup>( $\mu$ -OH)-( $\mu$ -piv)<sub>2</sub>(Me<sub>3</sub>tacn)<sub>2</sub>](ClO<sub>4</sub>)<sub>2</sub> (PivOH) complex is reported. It displays features that include: (i) a ground 1/2 spin state; (ii) a small exchange ( $J$ ) coupling between the two Mn ions; (iii) a mono- $\mu$ -hydroxo bridge, bis- $\mu$ -carboxylato motif; and (iv) a strongly coupled, terminally bound N ligand to the Mn<sup>III</sup>. All of these features are observed in structural models of the oxygen evolving complex (OEC). Multifrequency electron paramagnetic resonance (EPR) and electron nuclear double resonance (ENDOR) measurements

were performed on this complex, and the resultant spectra simulated using the Spin Hamiltonian formalism. The strong field dependence of the <sup>55</sup>Mn-ENDOR constrains the <sup>55</sup>Mn hyperfine tensors such that a unique solution for the electronic structure can be deduced. Large hyperfine anisotropy is required to reproduce the EPR/ENDOR spectra for both the Mn<sup>II</sup> and Mn<sup>III</sup> ions. The large effective hyperfine tensor anisotropy of the Mn<sup>II</sup>, a d<sup>5</sup> ion which usually exhibits small anisotropy, is interpreted within a formalism in which the fine structure tensor of the Mn<sup>III</sup> ion strongly perturbs the zero-field energy levels of the Mn<sup>II</sup>Mn<sup>III</sup> complex. An estimate of the fine structure parameter ( $d$ ) for the Mn<sup>III</sup> of  $-4\text{ cm}^{-1}$  was made, by assuming the intrinsic anisotropy of the Mn<sup>II</sup> ion is small. The magnitude of the fine structure and intrinsic (onsite) hyperfine tensor of the Mn<sup>III</sup> is consistent with the known coordination environment of the Mn<sup>III</sup> ion as seen from its crystal structure. Broken symmetry density functional theory (DFT) calculations were performed on the crystal structure geometry. DFT values for both the isotropic and the anisotropic components of the onsite (intrinsic) hyperfine tensors match those inferred from the EPR/ENDOR simulations described above, to within 5%. This study demonstrates that DFT calculations provide reliable estimates for spectroscopic observables of mixed valence Mn complexes, even in the limit where the description of a well isolated  $S = 1/2$  ground state begins to break down.



## 1. INTRODUCTION

Several  $\mu$ -oxo/hydroxo bridged Mn cofactors have been found in biological enzymes. Important examples include (a) the dimanganese catalase,<sup>1,2</sup> which catalyzes the dismutation of H<sub>2</sub>O<sub>2</sub> to H<sub>2</sub>O and O<sub>2</sub>; (b) the recently identified Mn containing class Ib ribonucleotide reductase;<sup>3,4</sup> and (c) the tetra-manganese oxygen evolving complex (OEC) of reference PSII which performs the multistep oxidation of H<sub>2</sub>O to O<sub>2</sub>. To understand the chemistry these complexes perform it is important to resolve, in detail, their geometric and electronic structures. Synthetic complexes play a crucial part in this exercise, allowing specific features to be examined separately. In multielectron-reactions such as water-splitting the catalysts must cycle through several different oxidation states, many of which are paramagnetic. As such, electron paramagnetic resonance (EPR) spectroscopy is

an invaluable tool for the elucidation of the properties of these complexes. Mixed valence complexes such as Mn<sup>II</sup>Mn<sup>III</sup> and Mn<sup>III</sup>Mn<sup>IV</sup>, typically exhibit antiferromagnetic coupling leading to the ground state configuration of total electron spin ( $S_T$ ) of 1/2. The  $S_T = 1/2$  state manifests itself in CW-EPR as a characteristic multiline signal centered at  $g \sim 2$ . The large number of spectral lines observed arises from the coupling of the two <sup>55</sup>Mn nuclei to the total unpaired electronic spin. In principle, the electronic structures can be derived from these measurements. However, the analysis of EPR spectra of exchange-coupled systems is often complicated by the presence of multiple terms of similar energetic importance in the spin Hamiltonian. In

Received: April 13, 2011

Published: August 11, 2011

general it is impossible to obtain unique parameters for the Hamiltonian from a single EPR spectrum. One solution to this problem is to measure the EPR spectrum at multiple frequencies (X-, Q-, and W-band). As the different components of the Spin Hamiltonian have different magnetic field dependence, this allows the relative contributions to be resolved.<sup>5,6</sup> An important complementary approach is electron nuclear double resonance (ENDOR) spectroscopy.<sup>7,8</sup> <sup>55</sup>Mn-ENDOR spectra are usually much simpler to analyze because of the lower number of overlapping transitions and its insensitivity to the exact geometry of the hyperfine tensors relative to each other. As a consequence, reliable information on the hyperfine couplings, and, to a lesser extent, nuclear quadrupole couplings of the <sup>55</sup>Mn ( $I = 5/2$ ) nuclei can be readily obtained using such measurements. In studies on mixed valence Mn<sup>III</sup>Mn<sup>IV</sup> complexes the combination of both multifrequency-EPR and <sup>55</sup>Mn-ENDOR has allowed not only a determination of the effective  $G$  and hyperfine tensors ( $A_1$ ,  $A_2$ ) but also their relative orientations. While there are multiple EPR/<sup>55</sup>Mn-ENDOR studies on synthetic and biological Mn<sup>III</sup>Mn<sup>IV</sup> complexes<sup>5,6,9–14</sup> all efforts, including our own, to obtain such measurements for Mn<sup>II</sup>Mn<sup>III</sup> complexes have failed thus far. The reason for this is the very fast  $T_1$  relaxation in such complexes.<sup>15</sup> As such only CW-EPR studies have yet been reported for Mn<sup>II</sup>Mn<sup>III</sup> model complexes.<sup>5,16–19</sup> Here we demonstrate for the first time that pulsed <sup>55</sup>Mn ENDOR measurements at Q-band frequency can be successfully employed for deriving the electronic structure of an exchange coupled Mn<sup>II</sup>Mn<sup>III</sup> complex. The complex used is the well characterized [Mn<sup>II</sup>Mn<sup>III</sup>( $\mu$ -OH)-( $\mu$ -piv)<sub>2</sub>(Me<sub>3</sub>tacn)<sub>2</sub>](ClO<sub>4</sub>)<sub>2</sub> (PivOH) complex previously reported by Bossek et al.<sup>20</sup> This complex contains a  $\mu$ -hydroxo ( $\mu$ -OH) and two  $\mu$ -carboxylato ( $\mu$ -piv) bridges between the two Mn ions (see Figure S). The oxidation states of the two Mn ions could be identified from the crystal structure because of the elongation of the Mn(2)–N(5) and Mn(2)–O(3) bonds. This elongation represents the Jahn–Teller axis of the Mn<sup>III</sup>.

Static magnetization measurements have estimated the exchange coupling between the two Mn ions as antiferromagnetic  $J = -8.5 \text{ cm}^{-1}$  with an unusually large on-site zero-field splitting for the Mn<sup>III</sup> ion,  $|d^{\text{III}}| = 8 \text{ cm}^{-1}$  (see ref 21). Subsequent pulse EPR measurements on frozen solution samples agree with this result;  $J$  was found to lie within  $-9.3$  to  $-8.2 \text{ cm}^{-1}$ , see ref 15. Thus this complex represents a system where the  $J$  coupling alone does not describe well the energy-levels of the system. A demonstration of how additional terms in the Spin Hamiltonian contribute to the total zero-field splitting of the complex and the experimental manifestation of these effects are discussed.

## 2. MATERIALS AND METHODS

**2.1. Magnetic Susceptibility Measurements.** Measurements were performed on powder samples of solid material in the temperature range 2–300 K by using a SQUID susceptometer with a field of 1.0 T (MPMS-7, Quantum Design, calibrated with standard a palladium reference sample, error <2%). Multiple-field variable-temperature magnetization measurements were done at 1 T, 4 T, and 7 T also in the range 2–300K with the magnetization equidistantly sampled on a  $1/T$  temperature scale. The experimental data were corrected for underlying diamagnetism by use of tabulated Pascal's constants,<sup>22,23</sup> as well as for temperature-independent paramagnetism. The susceptibility and magnetization data were simulated with the program julX for exchange coupled systems.<sup>24</sup> Simulations presented are based on the Spin

Hamilton formalism (see Theory section 3). The magnetic moments were obtained from the eigenfunctions  $\psi_i$  of the appropriate Spin Hamiltonian ( $\hat{H}$ ) by using the Hellman–Feynman theorem  $\vec{\mu}_i(\vec{B}) = -\langle \psi_i | d\hat{H}/d\vec{B} | \psi_i \rangle$  where  $\vec{B}$  denotes the applied magnetic field. Powder summations were done by using a 16-point Lebedev grid.<sup>25,26</sup> Intermolecular interactions were considered by using a Weiss temperature,  $\Theta_w$ , as perturbation of the temperature scale,  $kT' = k(T - \Theta_w)$  for the calculation.

**2.2. EPR Measurements.** Q-band CW-EPR measurements were performed using a Bruker ESR 200D spectrometer equipped with an Oxford Instruments ESR 935 cryostat and ITC4 temperature controller. For data acquisition and spectrometer control a computer was used running a lab-written control program. The microwave frequency and magnetic field strength were monitored using a Hewlett-Packard 5352B frequency counter and a Bruker ER035M NMR gaussmeter, respectively.

Q-band pulse EPR and <sup>55</sup>Mn-Davies ENDOR measurements were performed at 4.2 K using a Bruker ELEXSYS E580 Q-band pulse EPR spectrometer equipped with an Oxford-CF935 liquid helium cryostat and an ITC-503 temperature controller. Electron spin echo-detected (ESE) field-swept spectra were measured using the pulse sequence:  $\pi/2 - \tau - \pi - \tau - \text{echo}$ , where  $\pi = 80 \text{ ns}$  and  $\tau = 440 \text{ ns}$ . <sup>55</sup>Mn-Davies ENDOR spectra were collected using the pulse sequence:  $\pi - \pi_{\text{RF}} - T - \pi/2 - \tau - \pi - \tau - \text{echo}$ , where  $\pi = 80 \text{ ns}$ ,  $\tau = 440 \text{ ns}$ ,  $\pi_{\text{RF}}$  (RF pulse, radio frequency) =  $3.5 \mu\text{s}$  and a delay of  $T = 600 \text{ ns}$ . To measure hyperfine couplings larger than 150 MHz, an external home-built computer console (SpecMan4EPR control software<sup>12,27,28</sup>) was used with the ELEXSYS E580 Q-band pulse EPR spectrometer, coupled to an external RF generator (SMT02 signal generator) and RF amplifier (ENI 5100 L). A shot repetition rate of  $\sim 300 \text{ Hz}$  was used for all measurements. Mn-ENDOR experiments were performed using the random (stochastic) acquisition technique as described in Epel et al.<sup>29</sup> Usual sequential acquisition in this ENDOR experiment with the PivOH complex resulted in a severe distortion of the Mn-ENDOR spectrum caused by “heating artifacts”. This is described in more details in Kulik et al.<sup>8</sup>

**2.3. CW-EPR/<sup>55</sup>Mn-ENDOR Simulations.** CW-EPR/<sup>55</sup>Mn-ENDOR spectra were simultaneously fit assuming an effective spin  $S = 1/2$  ground state (see Theory section 3.2). The same Spin Hamiltonian was used for both CW-EPR and <sup>55</sup>Mn-ENDOR spectra. The electron Zeeman term was treated exactly. The nuclear Zeeman, hyperfine, and quadrupole terms were treated using second order perturbation theory. Spectral simulations were performed numerically using Scilab-4.4.1, an open source vector-based linear algebra package (www.scilab.org) and the EasySpin package<sup>30</sup> in MATLAB. Linewidths (fwhm) used for the simulations presented in Figures 1 and 2 are CW-EPR 6.5 MHz; Pulse-EPR 2.7 MHz; Pulse-ENDOR 5.0 MHz. An anisotropic line broadening was included in simulations with principal values [320 163 112] MHz. A Gaussian profile was used to describe the excitation line width, with a fwhm of 20 MHz.

**2.4. Computational Details.** **2.4.1. Geometry Optimizations.** Geometry optimizations used the BP86 density functional<sup>31,32</sup> along with the 2010 DFT dispersion corrections from Grimme et al.<sup>33</sup> and the zero-order regular approximation (ZORA) to account for relativistic effects.<sup>34–36</sup> The segmented all-electron relativistically contracted (SARC) def2-SVP basis sets were used for the hydrogen and carbon atoms while the SARC def2-TZVP(-f) basis sets were used for all other atoms.<sup>37</sup> Optimizations took advantage of the RI approximation with the decontracted auxiliary def2-TZVP/J Coulomb fitting basis sets<sup>38</sup> as implemented in ORCA.<sup>39</sup> Increased integration grids (Grid4 in ORCA convention) and tight SCF convergence criteria were used throughout.

**2.4.2. EPR Parameter Calculations.** The exchange coupling constant ( $J$ ), hyperfine tensors, and nuclear quadrupole tensors were calculated for the manganese ions and nitrogen atoms in each model of PivOH using

the broken-symmetry density functional theory (DFT) methodology (BS-DFT),<sup>40–43</sup> The hybrid meta-GGA TPSSH functional<sup>44</sup> was used with the chain-of-spheres (RJCOSX) approximation to exact exchange.<sup>45</sup> Scalar relativistic effects were included with ZORA paired with the SARC def2-TZVP(-f) basis sets and the decontracted def2-TZVP/J Coulomb fitting basis sets for all atoms. Increased integration grids (Grid4 and GridX4 in ORCA convention) and tight SCF convergence criteria were used in the calculation of all EPR parameters. For the calculation of the manganese hyperfine and quadrupole tensors specially constructed basis sets, based on SARC def2-TZVP, were used for the Mn, N, and O atoms. These basis sets contain fully decontracted s-shells with three additional steep primitives added to the core (details are presented in the Supporting Information S7). This construction is similar to that used previously in the Core Properties (CP) basis set,<sup>46</sup> with the benefit of being consistent with the ZORA method used. The integration grids were increased to an integration accuracy of 11 and 9 (ORCA convention) for Mn and N/O, respectively. Picture change effects were applied for the calculation of the <sup>55</sup>Mn hyperfine and quadrupole tensors. The application of the BS-DFT approach and the performance of the TPSSH functional for the calculation of exchange coupling constants and hyperfine coupling constants in manganese systems has been extensively discussed, benchmarked and calibrated in previous studies of manganese dimers,<sup>47–49</sup> trimers,<sup>50</sup> and tetramers.<sup>51,52</sup>

### 3. THEORY

**3.1. The Spin Hamiltonian Formalism.** Here we consider an antiferromagnetically exchange coupled Mn<sup>II</sup>Mn<sup>III</sup> dimer. A basis set that describes the Mn-dimer spin manifold can be built from the product of the eigenstates of the two interacting spins:

$$|S_1 S_2 M_1 M_2 I_1 I_2 m_1 m_2\rangle \quad (1)$$

Here  $S_i$  refers to the electronic spin state of Mn<sub>*i*</sub>,  $M_i$  refers to the electronic magnetic sublevel of Mn<sub>*i*</sub>,  $I_i$  refers to the nuclear spin state of Mn<sub>*i*</sub>, and  $m_i$  refers to the nuclear magnetic sublevel of Mn<sub>*i*</sub>.  $S_i$  takes the value  $5/2$  for Mn<sup>II</sup> and 2 for Mn<sup>III</sup>;  $M_i$  takes the values:  $S_i, S_i-1, \dots, 1-S_i, -S_i$ ;  $I_i$  takes the value  $5/2$  for <sup>55</sup>Mn (100% natural abundance) and;  $m_i$  takes the values  $-I_i, 1-I_i, \dots, I_i-1, I_i$ . The Spin Hamiltonian that describes the spin manifold of the Mn dimer is

$$\hat{H} = \sum_i \beta_e \vec{B}_0 \cdot \hat{g}_i \cdot \vec{S}_i - \sum_i g_n \beta_n \vec{B}_0 \cdot \vec{I}_i + \sum_i \vec{S}_i \cdot \hat{a}_i \cdot \vec{I}_i + \sum_i \vec{I}_i \cdot \hat{p}_i \cdot \vec{I}_i + \sum_i \vec{S}_i \cdot \hat{d}_i \cdot \vec{S}_i - 2\vec{S}_1 \cdot \hat{J} \cdot \vec{S}_2 \quad (2)$$

It contains (i) an electronic Zeeman term for each Mn ion; (ii) a nuclear Zeeman term for each <sup>55</sup>Mn nucleus; (iii) an electron–nuclear hyperfine term for each <sup>55</sup>Mn nucleus; (iv) a nuclear quadrupole term for each <sup>55</sup>Mn nucleus; (v) a fine structure term for each Mn ion; and (vi) a electron spin coupling term for the Mn–Mn interaction.

**3.2. Effective Spin 1/2 Ground State.** The electronic coupling between the two Mn ions in mixed valence Mn dimers is usually dominated by the through bond exchange interaction and sufficiently large that the spin manifold can be treated within the strong exchange limit. In this instance the exchange interaction between the two Mn ions is significantly larger than any other term of the Spin Hamiltonian. The resultant electronic spin states of the manifold are then adequately described by a single quantum number, the total spin ( $S_T$ ). The “multiline” EPR signal observed for the PivOH complex is derived from only one total spin state, the ground state of the spin manifold with total spin

$S_T = 1/2$ . The basis set that describes this subspace takes the form

$$\left| \frac{1}{2} \quad M \quad m_1 \quad m_2 \right\rangle \quad (3)$$

Where  $M$  takes all half-integer values  $-1/2 \leq M \leq 1/2$ ; and  $m_i$  (where  $i = 1-2$ ) takes all half integer values  $-5/2 \leq m_i \leq 5/2$ . The effective Spin Hamiltonian that describes the ground state of the spin manifold ( $S_T = 1/2$ ) is

$$\hat{H} = \beta_e \vec{B}_0 \cdot \hat{G} \cdot \vec{S} + \sum_i (g_n \beta_n \vec{B}_0 \cdot \vec{I}_i + \vec{S} \cdot \hat{A}_i \cdot \vec{I}_i + \vec{I}_i \cdot \hat{P}_i \cdot \vec{I}_i) \quad (4)$$

It contains (i) the electronic Zeeman term for the total electronic spin; (ii) nuclear Zeeman terms for each <sup>55</sup>Mn nucleus; (iii) electron–nuclear hyperfine terms for each <sup>55</sup>Mn nucleus, and (iv) nuclear quadrupole terms for each <sup>55</sup>Mn nucleus.

**3.3. Isotropic Spin Projections.** A mapping of the spin subspace in section 3.2 onto the original basis set as described in section 3.1 can be made. This was first described by Sage et al.<sup>53</sup> in relation to the dimeric iron cofactor of purple acid phosphatase and extended to mixed valence manganese complexes by Zheng et al.<sup>19</sup> and Peloquin et al.<sup>11</sup> This allows the intrinsic  $g$  and hyperfine tensors of the four Mn ions ( $g_i, a_i$ , see eq 2) to be calculated from the effective  $G$  and hyperfine tensors ( $A_i$ , see eq 4). For an exchanged coupled Mn<sup>II</sup>Mn<sup>III</sup> complex the effective  $g$ -factor  $G$ , hyperfine tensors  $A_i$ , and quadrupole tensors  $P_i$  are related to the parameters of the complete spin Hamiltonian of the exchange-coupled system<sup>53,54</sup> by the spin-projection coefficients, where the isotropic spin projection coefficients ( $\rho_1, \rho_2$ ) are defined as:

$$\rho_1(\text{Mn}^{\text{II}}) = \frac{S_1(S_1 + 1) - S_2(S_2 + 1) + S(S + 1)}{2S(S + 1)}$$

$$\rho_2(\text{Mn}^{\text{III}}) = \frac{S_2(S_2 + 1) - S_1(S_1 + 1) + S(S + 1)}{2S(S + 1)} \quad (5)$$

and effective  $G$  and hyperfine values ( $A_i$ ), assuming all  $g_i$  and  $a_i$  are isotropic:

$$G = \rho_1 g_1 + \rho_2 g_2 + \frac{\rho_1 \rho_2}{S J} (g_1 - g_2) [(3\rho_1 + 1)d_1 - (3\rho_2 + 1)d_2]$$

$$A_1 = \rho_1 a_1 - a_1 \frac{\rho_1 \rho_2}{S J} [(3\rho_1 + 1)d_1 - (3\rho_2 + 1)d_2]$$

$$A_2 = \rho_2 a_2 + a_2 \frac{\rho_1 \rho_2}{S J} [(3\rho_1 + 1)d_1 - (3\rho_2 + 1)d_2]$$

$$P_1 = p_1$$

$$P_2 = p_2 \quad (6)$$

For an Mn<sup>II</sup>Mn<sup>III</sup> dimer,  $S_{1(\text{Mn}^{\text{II}})} = 5/2$ ; and  $S_{2(\text{Mn}^{\text{III}})} = 2$  which gives isotropic spin projection values of  $\rho_1 = 7/3$  and  $\rho_2 = -4/3$ , respectively. In the limit where exchange coupling  $J$  is large, the above relations are approximately:  $G = 7/3 g^{\text{II}} - 4/3 g^{\text{III}}$ ,  $A^{\text{II}} = 7/3 a^{\text{II}}$ ,  $A^{\text{III}} = -4/3 a^{\text{III}}$ ,  $P^{\text{II}} = p^{\text{II}}$ ,  $P^{\text{III}} = p^{\text{III}}$ .<sup>13,53</sup>

**3.4. Anisotropic Spin Projections.** It is noted that the expressions above derived from first order perturbation theory break down in systems where  $J$  is not large. In systems that have a pseudo-well isolated ground state it is often more convenient to describe the spin projections  $\rho_i$  as a tensor as opposed to a scalar quantity, that is, the correction to the projected  $g$ /hyperfine tensor (second/third terms of eq 6) is subsumed into the spin projection coefficient itself. This formalism can also be readily generalized to

the large spin systems. Here the Mn ion fine structure terms are included in the Spin Hamiltonian that describes the spin manifold (total zero-field splitting) of the complex.

$$\hat{H} = -2J\vec{S}_1 \cdot \vec{S}_2 + \vec{S}_1 \cdot \hat{d}_1 \cdot \vec{S}_1 + \vec{S}_2 \cdot \hat{d}_2 \cdot \vec{S}_2 \quad (7)$$

The fine structure tensors are traceless and as such be expressed in terms of two parameters  $d_{1,2}$  and  $e_{1,2}$ :

$$\hat{d}_i = \begin{bmatrix} -\frac{1}{3}(d_i - 3e_i) & 0 & 0 \\ 0 & -\frac{1}{3}(d_i + 3e_i) & 0 \\ 0 & 0 & \frac{2}{3}d_i \end{bmatrix} \quad (8)$$

The projection of the total spin onto the individual Mn centers is defined as the ratio of the on-site spin expectation value  $\langle S_z^i \rangle$  of the  $i$ -th Mn to the “total spin”  $S_T$  or equally  $\langle S_z \rangle$ :<sup>51</sup>

$$\rho_i = \frac{\langle S_z^i \rangle}{\langle S_z \rangle} \quad \text{or} \quad \rho_i = \frac{\langle S_z^i \rangle}{S_T} \quad (9)$$

For the  $S_T = 1/2$  electronic spin-manifold the expectation value of the spin operator  $\langle S_z \rangle$  is  $1/2$  and thus eq 6 can be re-expressed as

$$\rho_i = 2 \cdot \langle S_z^i \rangle \quad (10)$$

The effective  $\hat{G}$  and hyperfine tensors ( $\hat{A}_i$ ) are a weighted, linear sum of the intrinsic  $g$  and hyperfine tensors ( $a_i$ ) of the individual Mn ions.

$$\begin{aligned} \hat{G} &= \hat{\rho}_1 \hat{g} + \hat{\rho}_2 \hat{g} \\ \hat{A}_1 &= \hat{\rho}_1 \hat{a}_1 \\ \hat{A}_2 &= \hat{\rho}_2 \hat{a}_2 \\ \hat{P}_1 &= \hat{p}_1 \\ \hat{P}_2 &= \hat{p}_2 \end{aligned} \quad (11)$$

**3.5. Calculation of Mn–Mn Exchange Couplings Using Broken Symmetry (BS) DFT.** The calculation of the exchange coupling ( $J$ ) was performed assuming the “isotropic” Heisenberg Hamiltonian shown below, that is, the same as eq 7 but excluding the fine structure terms.

$$\hat{H} = -2J\vec{S}_1 \cdot \vec{S}_2 \quad (12)$$

Within the formalism of BS-DFT the exchange coupling constant ( $J$ ) can be calculated in a number of ways. Here the method of Yamaguchi was used (eq 13), which has been shown to correctly estimate exchange couplings over the entire range of coupling regimes, that is, from the weak to strong coupling limit.<sup>55,56</sup>

$$J = -\frac{E_{\text{HS}} - E_{\text{BS}}}{\langle S^2 \rangle_{\text{HS}} - \langle S^2 \rangle_{\text{BS}}} \quad (13)$$

The calculation of the exchange coupling constants can be performed using either an adiabatic or a single geometry approach. For the adiabatic approximation of  $J$ , the energies and  $\langle S^2 \rangle$  values from both the optimized high-spin and broken-symmetry geometries are entered into eq 13. The more common approach is to simply use the high-spin and broken-symmetry energies and  $\langle S^2 \rangle$  values for a single geometry, usually optimized in the high-spin state. The adiabatic approximation is the better

representation of the measured exchange coupling as the experiments are inherently adiabatic.

**3.6. Hyperfine Couplings from Broken-Symmetry DFT.** A technique which allows for the extraction of hyperfine coupling constants from BS-DFT calculations was developed recently.<sup>51</sup> The approach was shown to give calculated <sup>55</sup>Mn hyperfine couplings that can be meaningfully compared with experimental values of manganese dimers,<sup>47–49</sup> trimers,<sup>50</sup> and tetramers.<sup>51,52</sup> The main concepts of the method will be highlighted here, for more detailed descriptions of the method see refs 51,52.

For a system composed of metal-centered subsystems, in this case subsystems centered on the Mn<sup>II</sup> and Mn<sup>III</sup> ions, the general equation linking the isotropic BS calculated hyperfine coupling constants to experiment is given below for a nucleus  $j$  within subsystem  $i$ .

$$A_{\text{iso}}^{(i,j)} = A_{\text{iso,site}}^{(i,j)} \frac{\langle S_z^{(i)} \rangle}{S_T} \quad (14)$$

where  $S_T$  is the effective total spin ( $1/2$ ),  $\langle S_z^{(i)} \rangle$  is the on-site spin expectation value, and  $A_{\text{iso,site}}^{(i,j)}$  is the site isotropic coupling constant defined as follows:

$$A_{\text{iso,site}}^{(i,j)} = A_{\text{iso,BS}}^{(j)} \frac{\langle S_z \rangle_{\text{BS}}}{S_i} \quad (15)$$

Here  $S_i$  is the site-spin of subsystem  $i$  and is positive or negative depending on whether the subsystem carries majority or minority spin.  $\langle S_z \rangle_{\text{BS}}$  is the total  $M_S$  of the BS wave function and  $A_{\text{iso,BS}}^{(j)}$  is the “raw” hyperfine coupling constant calculated directly from the BS calculation. The final projection of the site isotropic coupling constant into the correct effective hyperfine coupling constant is possible through the use of the isotropic spin projection coefficients,  $7/3$  and  $-4/3$  for Mn<sup>II</sup> and Mn<sup>III</sup>, or alternatively, the anisotropic spin-projection coefficients as described in the previous section. It has been previously established that calculations of hyperfine components of Mn are underestimated with the BS-DFT method and require an empirically determined scaling factor.<sup>47,48,51,52</sup> As the methodology used here differs from previous reports we redetermined the scaling factor to be 1.50 for the basis set and density functional used here. See the Supporting Information S8 for more information on the determination of the scaling factor.

## 4. RESULTS

**4.1. Magnetic Susceptibility.** Pure samples of the Mn<sup>II</sup>Mn<sup>III</sup> PIVOH complex used in this study were synthesized as described in ref 20. In the Supporting Information S1 the temperature dependence of the magnetic susceptibility of a powder sample of the PivOH complex recorded at an applied field of  $B_0 = 1$  T (plotted as  $\chi T$  vs  $T$ ) is shown. A small offset on the  $y$ -axis ( $\chi T$ ) is inferred and is assigned to a paramagnetic impurity. This impurity presumably represents the fraction of complexes which have decomposed to a monomeric Mn<sup>2+</sup> species (see section 4.2.1). The data could be readily modeled using the Spin Hamiltonian given in the Theory section 3.1 (eq 2). In these simulations only the electronic terms are considered. The nuclear terms (hyperfine, quadrupole) are sufficiently small, of the order of MHz, that they form no significant contribution to the total zero-field splitting of the complex, which is of the order of  $\text{cm}^{-1}$ . The simulation strongly depends on the signed magnitude of the exchange coupling  $J$ , estimated to be  $-8.6 \text{ cm}^{-1}$ . In contrast,

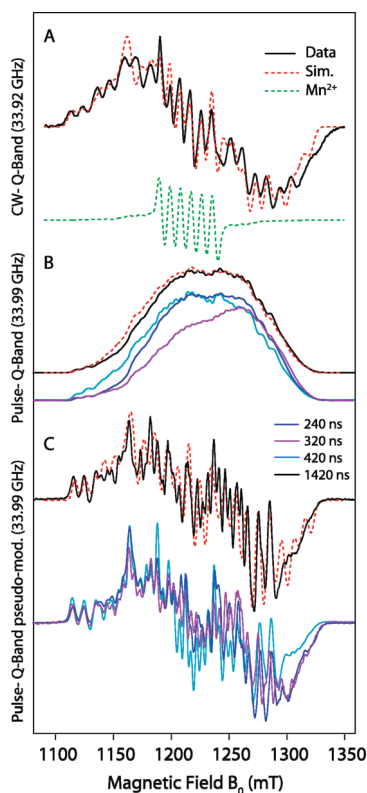


**Figure 1.** CW and pulsed Q-band EPR spectra of the  $\text{Mn}^{\text{II}}\text{Mn}^{\text{III}}$  PivOH complex. (A) CW-Q-band. Experimental parameters: microwave frequency: 33.92 GHz; microwave power: 8 mW; modulation amplitude: 0.2 mT, 1.5 kHz; temperature: 10 K. (B) Q-band pulse EPR, ESE-detected field sweep. Experimental parameters: microwave frequencies: 33.69 GHz; shot repetition rate: 5  $\mu\text{s}$ ; microwave pulse length ( $\tau$ ): 80 ns,  $\tau$ : 240 ns, 320 ns, 420 and 1420 ns, temperature: 4.2 K. (C) Corresponding pseudomodulated 'CW like' EPR lineshapes for the absorption spectra presented in panel B. These spectra were generated by convoluting the original absorption spectra with a Bessel function of the 1st kind. The peak-to-peak field modulation used was 3 mT. Solid lines represent the experimental data. The red dashed lines superimposing each data trace represent a least-squares fitting to the whole data set (see Figures 1 and 2) using a model based on the Spin Hamiltonian formalism (see Theory eq 4). It is noted that the CW-Q-band EPR spectrum contains a small contribution of free  $\text{Mn}^{2+}$ . In solution  $\text{Mn}^{2+}$  usually appears as a narrow EPR signal centered at  $g \sim 2$ , with 6 sharp peaks with peak-to-peak separation of 8–10 mT. The contribution of the  $\text{Mn}^{2+}$  signal is shown by the green dashed traces and is included in the simulation profile shown by the red dashed traces. All fitting parameters are given in Table 1.

the fine structure parameters of both Mn ions ( $d_1$ ,  $d_2$ ) are not well-defined. This is plausible because the ground state is a doublet, without zero-field splitting and the splitting in the excited manifolds should barely affect the values of  $\chi T$ . An error correlation diagram for the exchange coupling constant  $J$  and the fine structure parameter  $d_2$  of Mn(III) as shown in the Supporting Information S1 which shows this feature of the static magnetic measurements.

**4.2. EPR Spectroscopy.** **4.2.1. CW EPR.** The CW-Q-band EPR frozen solution spectrum of the  $\text{Mn}^{\text{II}}\text{Mn}^{\text{III}}$  PivOH complex is shown in Figure 1A. The samples were dissolved in a mixture of purified dry  $\text{CH}_3\text{CN}$  and  $\text{CH}_2\text{Cl}_2$  (1:3 v/v) at a concentration of  $\sim 1$  mM. This solvent combination was previously seen to impart

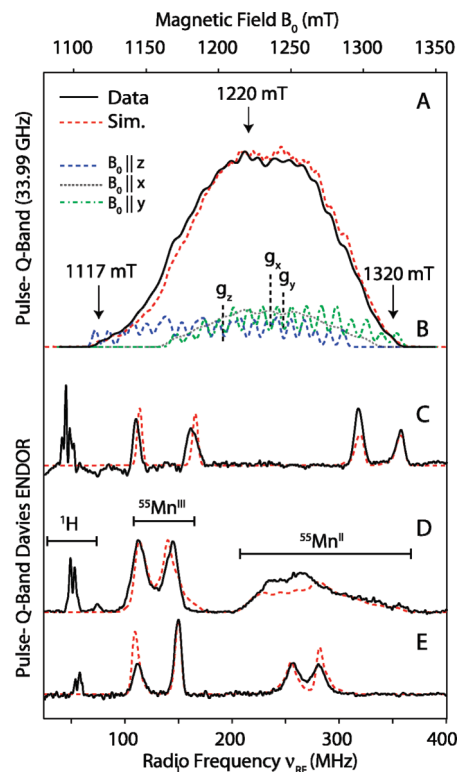


**Figure 2.** Pulsed Q-band EPR and ENDOR spectra of the  $\text{Mn}^{\text{II}}\text{Mn}^{\text{III}}$  PivOH complex. (A) Q-band pulse EPR, ESE-detected field sweep (as shown in Figure 1B). (B) A decomposition of the EPR simulation along the three principal axes,  $x$ ,  $y$ , and  $z$ . (C, D, and E)  $^{55}\text{Mn}$ -ENDOR spectra collected at three field positions within the EPR absorption profile: 1117 mT, 1220 mT, and 1320 mT, respectively. The black, solid line represents the experimental data. The red dashed lines superimposing each data trace represent a least-squares fitting to the whole data set (see Figures 1 and 2) using a model based on the Spin Hamiltonian formalism (see Theory eq 4). The optimized parameter sets are given in Table 1. The contribution of the  $\text{Mn}^{\text{II}}$  and  $\text{Mn}^{\text{III}}$  ions to the  $^{55}\text{Mn}$ -ENDOR spectra is shown by the black bars.

good relaxation properties ( $T_1$ ,  $T_2$ ). The spectrum is centered at  $g \sim 1.97$ , and it contains at least 23 spectral lines spread over a field range of 220 mT. The hyperfine line spacing is of the order of 10–12 mT, as estimated from the spectral lines at the low and high field edges of the spectrum. The center of the hyperfine pattern has a slightly different hyperfine spacing suggesting a small contamination from a monomeric  $\text{Mn}^{2+}$  species. Monomeric  $\text{Mn}^{2+}$  typically manifests itself as a "six line" EPR signal, centered at  $g \sim 2.0$ , with hyperfine line spacing of  $\sim 9$  mT. The estimated contribution of the  $\text{Mn}^{2+}$  species is shown by the black dashed line (Figure 1A).

The spectral pattern observed for the  $\text{Mn}^{\text{II}}\text{Mn}^{\text{III}}$  PivOH complex is typical of antiferromagnetically coupled, mixed valence manganese dimers ( $\text{Mn}^{\text{III}}\text{Mn}^{\text{II}}/\text{Mn}^{\text{III}}\text{Mn}^{\text{IV}}$ ). The coupled Mn dimer can be treated as an effective spin 1/2 state, where the inhomogeneous line width of the spectrum (the total spectral breadth) is defined by the  $^{55}\text{Mn}$  hyperfine couplings of the two Mn nuclei to the fictitious electron spin  $S_T = 1/2$ . The  $G$ -tensor anisotropy of such systems is typically small and not resolved at low microwave frequencies (X, Q-band); that is to say the  $G$ -anisotropy is smaller than the line-broadening/line-splitting due to the hyperfine interaction. Regardless, an estimate can

be made of the  $G$ -anisotropy by comparing the total spectral breadth of the spectrum measured at both X and Q-band frequencies. The CW-X-band EPR spectrum of the  $\text{Mn}^{\text{II}}\text{Mn}^{\text{III}}$  **PivOH** complex was previously reported in refs 5,57 with total spectral breadth of  $\sim 180$  mT. This is approximately 40 mT narrower than that measured at Q-band. As the  $G$ -tensor is the only term of the effective Spin Hamiltonian (eq 4) that is dependent on the magnetic field, the increase in the total spectral breadth of the signal measured at the Q-band is a direct measure of the  $G$ -anisotropy. Thus a  $\Delta G$  of  $\sim 0.1$  is inferred, where  $\Delta G$  represents the difference between the largest and smallest component of the  $G$ -tensor, as seen for previous  $\text{Mn}^{\text{II}}\text{Mn}^{\text{III}}$  model complex studies.<sup>5,19,57</sup>

Pulse-Q-band EPR spectra of the  $\text{Mn}^{\text{II}}\text{Mn}^{\text{III}}$  **PivOH** complex are shown in Figure 1B. These spectra were detected using a Hahn-echo detection sequence ( $\pi/2$ - $\tau$ - $\pi$ - $\tau$ -echo) with varying pulse spacing of  $\tau = 240$  ns, 320 ns, 420 and 1420 ns. At each of these pulse spacings ( $\tau$ ) a different absorption line shape is observed. This is due to the large  $^{14}\text{N}$  hyperfine couplings of the Mn ligands (see Figure 5), which modulate the detected Hahn-echo as the magnetic field is swept (see ref 58 and references therein). This effect can be partially suppressed by using longer  $\tau$  values. Importantly, the total spectral breadth for all pulse spectra is the same and approximately that seen using CW-EPR. It is noted that the exact frequency of the CW-Q-band spectrum was calibrated such that the edges of the spectral envelope matched in the CW and pulse experiments. The corresponding pseudomodulated "CW-like" spectra are shown in Figure 1C. These spectra were generated by convoluting the original pulse (absorption) spectra with a Bessel function of the first kind. The hyperfine pattern observed is similar, but not identical to the CW spectrum. This appears to be mainly due to a difference in the line width. Spectral simulations are described in section 4.2.3.

The absorption lineshapes for pulse Q-band spectra regardless of the values of  $\tau$  (Figure 1B) are not Gaussian, but instead are skewed such that the spectra are elongated on their low field edge. This observation is consistent with a pseudo axial  $G$ -tensor of large anisotropy, as described above, and suggests the unique axis ( $z$ -component) of the  $G$ -tensor ( $G_z$ ) is larger than that the other two components ( $G_x$  and  $G_y$ ). This result is expected for  $\text{Mn}^{\text{II}}\text{Mn}^{\text{III}}$  complexes and has been previously inferred from spectral simulations of CW-EPR data (see section 4.2.4). It is pointed out that this feature of the **PivOH** complex can be demonstrated simply by using a higher frequency pulse-EPR experiment without the need to perform any spectral simulation. It should be noted that the inverse is seen for  $\text{Mn}^{\text{III}}\text{Mn}^{\text{IV}}$  complexes; the unique axis,  $G_z$ , is always smallest in these systems.<sup>5,6,9–14</sup>

**4.2.2.  $^{55}\text{Mn}$ -ENDOR.** Pulsed-Q-band Davies  $^{55}\text{Mn}$ -ENDOR spectra of the  $\text{Mn}^{\text{II}}\text{Mn}^{\text{III}}$  **PivOH** complex are shown in Figure 2. Spectra were recorded at the center of the absorption envelope (powder position) and at the low and high field edges of the absorption envelope (single crystal orientations). ENDOR signals assigned to the two  $^{55}\text{Mn}$  nuclei are observed over the 100–380 MHz range. Additional signals are seen in the region of 40–70 MHz. These are assigned to  $^1\text{H}$  nuclei associated with the  $\text{Mn}^{\text{II}}\text{Mn}^{\text{III}}$  **PivOH** complex, for example the  $\mu$ -hydroxo proton, see Figure 5.

$\text{Mn}^{\text{II}}$ ,  $\text{Mn}^{\text{III}}$ , and  $\text{Mn}^{\text{IV}}$  complexes typically resolve ENDOR signals across a large radio frequency range. At all obtainable microwave frequencies available (X, Q, W-band etc), the hyperfine coupling of the  $^{55}\text{Mn}$  nuclei is significantly larger than that of the  $^{55}\text{Mn}$  Larmor frequency. As such,  $^{55}\text{Mn}$ -ENDOR spectral

lines appear at about half the hyperfine coupling ( $a/2$ ) split by the nuclear Zeeman interaction.<sup>59</sup> The magnitude of the  $^{55}\text{Mn}$  quadrupole couplings is 2 orders of magnitude smaller than the hyperfine coupling and as such has only a small effect on the  $^{55}\text{Mn}$ -ENDOR spectrum. Onsite  $^{55}\text{Mn}$  hyperfine couplings ( $a$ ) for  $\text{Mn}^{\text{II}}$ ,  $\text{Mn}^{\text{III}}$ , and  $\text{Mn}^{\text{IV}}$  monomeric, dimeric, and tetramer complexes in the current literature all fall within the range 140–260 MHz, and as such  $^{55}\text{Mn}$ -ENDOR signals are expected for the  $\text{Mn}^{\text{II}}\text{Mn}^{\text{III}}$  **PivOH** complex between 70 and 130 MHz, that is,  $a/2$ . It can be clearly observed in Figure 2 that this is not the case; experimentally  $^{55}\text{Mn}$ -ENDOR signals extend to 380 MHz. The reason for this is that the effective hyperfine parameters of the coupled cluster measured in the EPR experiment represent scaled versions of the onsite (or intrinsic) hyperfine parameters of the two Mn ions. These scaling factors or spin projections (see Theory section 3.3-3.4) result in a spreading of the  $^{55}\text{Mn}$ -ENDOR spectrum across a larger frequency range. It is noted that the isotropic spin projections for the  $\text{Mn}^{\text{II}}$  and  $\text{Mn}^{\text{III}}$  ions ( $7/3$  and  $-4/3$ , respectively) are sufficiently different such that the  $^{55}\text{Mn}$ -ENDOR signals arising from the  $\text{Mn}^{\text{II}}$  and  $\text{Mn}^{\text{III}}$  nuclei are spectrally resolved. This is shown by the black bars in Figure 2D. This same basic phenomenology has been observed for mixed valence  $\text{Mn}^{\text{III}}\text{Mn}^{\text{IV}}$  complexes, see refs 5,6,9–14. Spectrum D represents the powder position. Here all orientations contribute approximately equally to the  $^{55}\text{Mn}$ -ENDOR signal. The spectral breadth of the  $\text{Mn}^{\text{III}}$  ENDOR signal is approximately 3 times smaller than that of the  $\text{Mn}^{\text{II}}$  ENDOR signal. An increase in the spectral breadth of the  $\text{Mn}^{\text{II}}$  ion is expected as it carries the larger spin projection, and this increase can be estimated by taking the ratio of the two isotropic spin projections, that is,  $7/3:4/3 = 1^3/4$ . This is approximately 2 times smaller than that seen experimentally suggesting the effective hyperfine tensor associated with the  $\text{Mn}^{\text{II}}$  ion is intrinsically more anisotropic than that of the  $\text{Mn}^{\text{III}}$ . This surprising result is discussed further in section 4.1.4.

The magnitude of the effective hyperfine tensor components along the three principal axes ( $x, y, z$ ) for the  $\text{Mn}^{\text{II}}$  and  $\text{Mn}^{\text{III}}$  ions can be deduced from the  $^{55}\text{Mn}$ -ENDOR spectra (C and E) collected at the low and high field edge of the absorption envelope respectively. The low field edge, which here is defined by  $G_z$ , displays the largest hyperfine tensor component ( $A_z$ ) for the effective hyperfine tensor associated with  $\text{Mn}^{\text{II}}$  and is estimated as  $\sim 670$  MHz; twice the midpoint of the doublet that appears between 320 and 360 MHz. Similarly, the  $\text{Mn}^{\text{III}}$   $A_z$  component is estimated to be 270 MHz. In contrast, the high field edge which is here defined by  $G_y$ , that appears to define the middle component of the  $\text{Mn}^{\text{II}}$  hyperfine tensor, is estimated to be  $\sim 540$  MHz. The corresponding  $\text{Mn}^{\text{III}}$  hyperfine component is  $\sim 260$  MHz. The  $\text{Mn}^{\text{II}}$  hyperfine tensor component along  $G_x$  can thus be deduced from the powder pattern spectrum. It must be of the order of  $\sim 450$  MHz to explain the low-frequency edge of the  $\text{Mn}^{\text{II}}$ -ENDOR signal, not seen at either of the single crystal orientations. The corresponding  $\text{Mn}^{\text{III}}$  hyperfine component is  $\sim 260$  MHz.

Radio-frequency nutation curves for three positions within the  $^{55}\text{Mn}$ -ENDOR spectrum are shown in Figure 3. It is readily observed across the 100–400 MHz radio frequency range, that the optimal  $\tau_{\text{rf}}$  pulse length for the  $^{55}\text{Mn}$ -ENDOR experiment varies. From these results the effective  $B_2$  (rf) field was estimated throughout the  $^{55}\text{Mn}$ -ENDOR signal envelope. As expected the  $B_2$  field falls off at high frequencies, leading to a partial suppression of  $^{55}\text{Mn}$  signals above 250 MHz. More unexpectedly, the  $B_2$

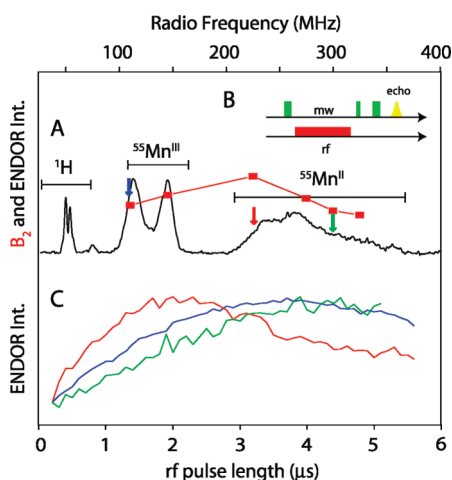


**Figure 3.**  $^{55}\text{Mn}$ -ENDOR intensity profile of the  $\text{Mn}^{\text{II}}/\text{Mn}^{\text{III}}$  PivOH complex. (A) Q-band pulse  $^{55}\text{Mn}$ -ENDOR spectrum collected at the central field position 1220 mT of the EPR absorption profile. The superimposed red squares show the effective  $B_2$  (rf) field. (B) The Davies ENDOR microwave and radiowave pulse sequence. (C) Radio-frequency nutation curves for the three  $^{55}\text{Mn}$ -ENDOR positions marked with the colored arrows. The contribution of the  $\text{Mn}^{\text{II}}$  and  $\text{Mn}^{\text{III}}$  ions to the  $^{55}\text{Mn}$ -ENDOR spectra is shown by the black bars.

field also drops at low frequency, a consequence of the decrease in the hyperfine enhancement factor. The net consequence of this is that the relative line-intensities of  $^{55}\text{Mn}$ -ENDOR signals reported are only an approximation of the real line-intensities as they in part reflect the response of the instrument. It is noted though that although the ENDOR signals are dampened at either end of the radiofrequency range probed, none of the signal envelope is completely suppressed.

**4.2.3. Spectral Simulations.** Spectral simulations of the entire data set were performed using the Spin Hamiltonian formalism described in the Theory section. Simulations of the data are shown in Figures 1 and 2, see red-dashed lines. All simulation parameters are given in Table 1. More emphasis was placed on reproducing the pseudomodulated derivative spectrum than the corresponding CW-line shape as the pulse spectra resolved more hyperfine structure and was free from  $\text{Mn}^{2+}$  artifacts. The isotropic line width used for the pulse and CW simulations differed by a factor of 2. An anisotropic line width broadening was included in the simulation that presumably accounts for unresolved hyperfine couplings ( $^{14}\text{N}$  etc), see Materials Methods 2.2.

The semiquantitative estimates of the Spin Hamiltonian parameters given in sections 4.2.1–4.2.2 all approximately agree with the fitted values. Single crystal orientation EPR simulations, solved for  $B_0$  aligned along the three principal axes ( $x$ ,  $y$ ,  $z$ ) are shown in Figure 2B. As expected, the single crystal orientation for which  $B_0$  coincides with the molecular  $z$ -axis, is the broadest, spanning 1116–1285 mT and defines the low-field of the spectral envelope. Similarly, the single crystal orientation where  $B_0$  coincides with the molecular  $y$ -axis, is narrower, spanning 1171–1322 mT and defines the high-field edge of the spectrum. The single crystal orientation where  $B_0$  coincides with the molecular  $x$ -axis, is narrower still and is located in the center of the spectral envelope, 1170–1300 mT. This requires  $G_z > G_x > G_y$ , and the  $\text{Mn}^{\text{II}}$  hyperfine tensor components to be  $|A_z| > |A_y| > |A_x|$ .

**Table 1.** Principal Values of the Effective  $G$  and  $^{55}\text{Mn}$  Hyperfine Tensors for the Simulations of the  $\text{Mn}^{\text{II}}/\text{Mn}^{\text{III}}$  PivOH Complex<sup>a</sup>

	spin hamiltonian parameters							
	G	hyperfine (MHz)					quadrupole ( $P$ , MHz)	
		projected ( $A_i$ )		intrinsic ( $a_i$ )			$\text{Mn}^{\text{II}}$	$\text{Mn}^{\text{III}}$
	$\text{Mn}^{\text{II}}$	$\text{Mn}^{\text{III}}$	$\text{Mn}^{\text{II}}$	$\text{Mn}^{\text{III}}$	$\text{Mn}^{\text{II}}$	$\text{Mn}^{\text{III}}$		
x	1.964	−453	255	−240	−287	−3.24	1.50	
y	1.947	−544	279	−239	−218	2.80	3.00	
z	2.022	−696	260	−240	−137	0.44	−4.00	
iso ( $P$ )	1.978	−564	264	−240	−214	−1.62	−2.00	
aniso ( $\eta$ )	0.066	−207	−7	−1	116	0.73	0.38	

<sup>a</sup> The isotropic  $G_{\text{iso}}$  and  $A_{i, \text{iso}}$  ( $i = 1-2$ ) values are the average of the individual values:  $G_{\text{iso}} = (G_x + G_y + G_z)/3$  and  $A_{i, \text{iso}} = (A_{i,x} + A_{i,y} + A_{i,z})/3$ . The perpendicular and parallel  $G$  and  $A_i$  values are defined as  $G_{\perp} = (G_x + G_y)/2$ ,  $G_{\parallel} = G_z$  and  $A_{i,\perp} = (A_{i,x} + A_{i,y})/2$ ,  $A_{i,\parallel} = A_{i,z}$ . The anisotropy in the  $\hat{G}$  and  $\hat{A}_i$  values is expressed as the difference between the parallel and perpendicular component of the tensor. The nuclear quadrupole coupling constant  $P$  is defined as:  $P = (e^2qQ)/(4hI(2I - 1)) = (P_3/2)$  and  $\eta = (P_1 - P_2)/(P_3)$ .  $P_1$ ,  $P_2$ , and  $P_3$  are defined such that  $|P_1| \leq |P_2| < |P_3|$ . As a consequence, the axis system for the quadrupole tensors of the  $\text{Mn}^{\text{II}}$  and  $\text{Mn}^{\text{III}}$  ions are different. Their principal axes are rotated  $90^\circ$  relative to each other. The intrinsic hyperfine tensor components ( $a_i$ ) are equal to the projected hyperfine tensor components ( $A_i$ ) divided by the spin projection coefficients  $\rho_i$  as defined in the Theory section. The spin projection coefficients  $[\rho_x, \rho_y, \rho_z]$  for the  $\text{Mn}^{\text{II}}$  and  $\text{Mn}^{\text{III}}$  ion are  $\text{Mn}^{\text{II}} = [1.90 \ 2.28 \ 2.89]$  and  $\text{Mn}^{\text{III}} = [-0.90 \ -1.28 \ -1.89]$ .

The simultaneous fitting of both the EPR and ENDOR data did not require an axis rotation of the  $\text{Mn}^{\text{II}}/\text{Mn}^{\text{III}}$  hyperfine tensors relative to the  $G$ -tensor. The simulations shown in the text assume the  $G$  tensor, hyperfine tensors  $A_1$  and  $A_2$  and quadrupole tensors  $Q_1$  and  $Q_2$  are collinear. It can be seen in Figure 5 that there is no structural requirement for this to be the case, the ligand sphere of the two metal ions is such that all components of the onsite axis system of the  $\text{Mn}^{\text{III}}$  do not coincide with the  $\text{Mn}^{\text{II}}$  ion. A three Euler angle rotation ( $\alpha = 53^\circ$ ,  $\beta = 81^\circ$ ,  $\gamma = 48^\circ$ ) is required to map the onsite axis system of the  $\text{Mn}^{\text{III}}$  to the  $\text{Mn}^{\text{II}}$ . This is a unique feature of the PivOH complex. All current EPR/ENDOR studies of mixed valence Mn dimers have been performed on complexes which contain a bridging network that enforces a common onsite axis system, such as the bis- $\mu$ -oxo bridge template.<sup>6,9,11,57,60</sup> Simulations that included an axis rotation are shown in the Supporting Information S3. In contrast to the hyperfine tensors, it was found that to reproduce the high frequency (250–400 MHz)  $^{55}\text{Mn}$  ENDOR, a rotation of the  $\text{Mn}^{\text{II}}$  quadrupole tensor was required. This rotation consisted of a permutation of the principal values of the tensor, that is, corresponded to a  $90^\circ$  rotation of the quadrupole tensor. The same rotation was not required for the  $\text{Mn}^{\text{III}}$  ion. Both of these observations can be readily explained and stem from the effective Spin Hamiltonian description used to model the system.

**4.2.4. Calculation of the Onsite (Intrinsic) Spin Hamiltonian Parameters.** A mapping of the effective (fitted) Spin Hamiltonian parameters described in section 4.2.3 to the onsite (intrinsic) Spin Hamiltonian parameter can be made for the  $\text{Mn}^{\text{II}}/\text{Mn}^{\text{III}}$  PivOH complex as described in the Theory section 3.3–3.4.

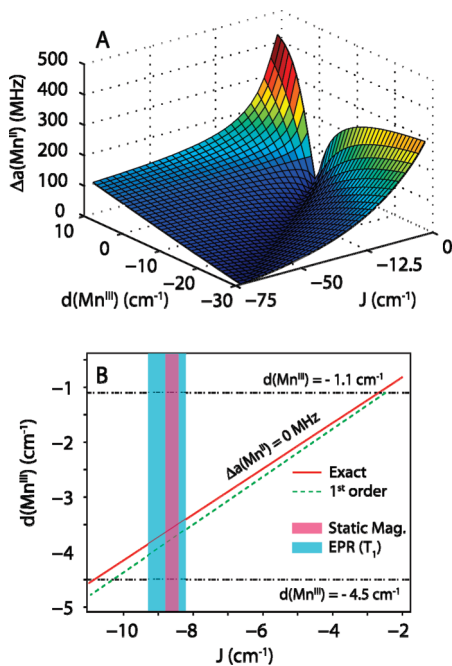


**Figure 4.** (A) Surface of the anisotropy of the onsite  $\text{Mn}^{\text{II}}$  hyperfine tensor ( $\Delta a_{\text{aniso}}$ ) as a function of both the  $\text{Mn}^{\text{II}}\text{--Mn}^{\text{III}}$  exchange interaction ( $J$ ) and the onsite fine structure parameter of the  $\text{Mn}^{\text{III}}$  ion  $d(\text{Mn}^{\text{III}})$ . (B) The projection of the surface shown in panel A, where the  $\Delta a_{\text{aniso}}(\text{Mn}^{\text{II}})$  is approximately zero. The trend is linear over the range  $-2$  to  $-10\text{ cm}^{-1}$ , consistent with the eq 6. The onsite fine structure tensor for the  $\text{Mn}^{\text{II}}$  ion was assumed to be  $0\text{ cm}^{-1}$  for all calculations.

The procedure described here is similar to that reported earlier.<sup>11,19,53,60</sup> This mapping requires knowledge of all contributions to the zero-field splitting of the coupled dimer, namely, an estimate of the exchange coupling between the two Mn ions and an estimate of the fine structure tensors for both Mn ions. As stated in the Introduction, good estimates exist for the exchange coupling between the two Mn ions. Static magnetization measurements reported earlier in Bossek et al.<sup>20</sup> and repeated here (see Section 4.1) yield a value of  $-8.6\text{ cm}^{-1}$  consistent with that previously reported by Kulik et al.,<sup>15</sup> as estimated from the temperature dependence of the  $T_1$  relaxation time using pulse-EPR experiments.<sup>15</sup> Similar reliable estimates do not exist for the fine structure tensors of the two Mn ions and as such, a unique mapping of the effective parameter space to the intrinsic parameter space can not be made without further restrictions. Here we use two key assumptions that pertain to the nature of  $\text{Mn}^{\text{II}}$  which is a  $d^5$ ,  $^6\text{S}$  ion ( $S = 5/2$ ). As all of the  $d$ -orbitals on  $\text{Mn}^{\text{II}}$  are half filled it can be expected that the valence electron shell is approximately spherically symmetric. This electronic configuration typically engenders small fine structure and hyperfine tensor anisotropy.<sup>61</sup> Literature values for the anisotropy of the fine structure and hyperfine tensors of  $\text{Mn}^{\text{II}}$  complexes are of the order of 1000 MHz. Of particular relevance are the dimeric equivalent  $\text{Mn}^{\text{II}}\text{Mn}^{\text{II}}$  complexes which contain a similar bridging template as seen for the **PivOH** complex. For these model systems small values have been reported for the effective zero-field splitting tensors of the  $S_T = 1$  and  $S_T = 2$  spin manifolds, consistent with the dipolar interaction between the two  $\text{Mn}^{\text{II}}$  ions dominantly defining the zero-field splitting within these manifolds,<sup>62</sup> that is, the

contribution of the onsite  $\text{Mn}^{\text{II}}$  fine structures to the zero field splitting is small. Thus it is expected that the contribution of the fine structure tensor of the  $\text{Mn}^{\text{II}}$  ion to the zero-field splitting of the **PivOH** complex is negligible<sup>63–65</sup> and that the anisotropy of its onsite hyperfine tensor should be small. It is these two properties that can be used as constraints to solve the remaining Spin Hamiltonian parameters, namely, the onsite fine structure and hyperfine tensors for the  $\text{Mn}^{\text{III}}$  ion.

The calculation of the onsite (intrinsic) Spin Hamiltonian parameters amounts to determining the spin projection coefficients for the two Mn ions. The spin projection coefficients are described in detail in the theory section. They can be thought of simply as scaling factors which take into account the effect of the exchange coupling ( $J$ ) and the fine structure tensors ( $d_1$  and  $d_2$ ) in the coupled basis. Spin projection coefficients were calculated numerically (see Theory eqs 7–11). The anisotropy of the exchange interaction was considered to be small and was thus not included in the calculations. The dipole–dipole coupling between the two manganese centers is of the order of 1200 MHz ( $0.04\text{ cm}^{-1}$ ).

The solution space for the onsite anisotropy ( $\Delta a_{\text{aniso}} = a_{\parallel} - a_{\perp}$ ) of the  $\text{Mn}^{\text{II}}$  ion as function of both the exchange coupling and the onsite fine structure parameter ( $d$ ) of the  $\text{Mn}^{\text{III}}$  ion is shown in Figure 4A. Each point on the surface represents a different estimate for the spin projections of the two Mn ions and thus a different estimate for the onsite  $\text{Mn}^{\text{II}}/\text{Mn}^{\text{III}}$  hyperfine tensor. This figure was generated by assuming the fine structure parameter  $d$  for the  $\text{Mn}^{\text{II}}$  ion was zero and by approximating the effective (fitted) hyperfine tensor of the  $\text{Mn}^{\text{II}}$  as axial. This approximation is simply used to conveniently display the onsite anisotropy surface. An estimate of the rhombicity of the fine structure tensor was also made.

It is observed that there is no unique solution as no global minimum can be identified (Figure 4A). Instead, a trough is observed, such that for every choice of  $J$  there is a value for  $d(\text{Mn}^{\text{III}})$  that is consistent with a virtually isotropic onsite  $\text{Mn}^{\text{II}}$  hyperfine tensor. The 2D projection of this solution is shown in Figure 4B. There is a clear linear dependence of  $d(\text{Mn}^{\text{III}})$  on the value of  $J$  over the range  $-10$  to  $-2\text{ cm}^{-1}$  range. This behavior is the same as predicted by the analytical expressions (eq 6) given in the theory section that has been derived from first order perturbation theory (see Supporting Information S2). The first order solution is also shown in Figure 4B (green dashed line). It is slightly offset from the numerical solution (red line), overestimating the magnitude of  $d(\text{Mn}^{\text{III}})$ . This offset presumably describes the contribution of higher order terms to the total zero-field splitting of the complex. As  $J$  for the **PivOH** complex has already been determined,<sup>15</sup> an estimate of  $d(\text{Mn}^{\text{III}})$  can be made. The EPR experimental range of  $J$  ( $-8.2$  to  $-9.3\text{ cm}^{-1}$ ) is shown in Figure 4B by the cyan shaded area and corresponds to  $d(\text{Mn}^{\text{III}})$  of  $-3.49$  to  $-3.95\text{ cm}^{-1}$ .

Table 1 also lists the calculated onsite hyperfine parameters for  $\text{Mn}^{\text{II}}$  and  $\text{Mn}^{\text{III}}$  at the midpoint of the allowed range of  $J$ , that is,  $J = -8.78\text{ cm}^{-1}$ ,  $d(\text{Mn}^{\text{III}}) = -3.72\text{ cm}^{-1}$ ,  $e/d(\text{Mn}^{\text{III}}) = 0.315$ . By design, this point yields an isotropic  $\text{Mn}^{\text{II}}$  hyperfine tensor with isotropic component ( $a_{\text{iso}}(\text{Mn}^{\text{II}})$ ) of  $-239\text{ MHz}$ , typical of  $\text{Mn}^{\text{II}}$  complexes. Similarly, the isotropic component of the onsite  $\text{Mn}^{\text{III}}$  hyperfine tensor ( $a_{\text{iso}}(\text{Mn}^{\text{III}})$ ) is  $-213\text{ MHz}$  and is within the range seen for model complexes ( $-165$  to  $-225\text{ MHz}$ ). Unlike the  $\text{Mn}^{\text{II}}$  onsite hyperfine tensor, the  $\text{Mn}^{\text{III}}$  hyperfine tensor is highly anisotropic, as expected. Furthermore, the anisotropy as defined by the difference between the parallel and the perpendicular components of the hyperfine tensor is positive, consistent with the sign of the inferred fine structure

tensor, that is,  $d(\text{Mn}^{\text{III}})$ . Thus the anisotropy of the two Mn ions in the coupled representation (section 4.2.3) is reversed when mapped to the original basis. A similar “transfer of anisotropy” has been previously observed in  $^{55}\text{Mn}$ -ENDOR studies of  $\text{Mn}^{\text{III}}\text{Mn}^{\text{IV}}$  complexes<sup>11,60</sup> albeit somewhat smaller and was inferred from simulations in the cw-EPR study of  $\text{Mn}^{\text{II}}\text{Mn}^{\text{III}}/\text{Mn}^{\text{III}}\text{Mn}^{\text{IV}}$  complexes by Zheng et al.<sup>19</sup>

The sign of the fine structure tensor parameter  $d(\text{Mn}^{\text{III}})$  accurately describes the coordination sphere of the  $\text{Mn}^{\text{III}}$  ion.  $\text{Mn}^{\text{III}}$  ( $S = 2$ ) is a  $d^4$  ion, which does not usually exhibit Kramers degeneracy at zero-field.<sup>19,61,66,67</sup> The inherent asymmetry of the valence electron configuration leads to a large Jahn–Teller distortion. Spin–orbit coupling removes the degeneracy of the  $^5\text{E}_g$  energy-levels, which gives rise to either a  $^5\text{A}_{1g}$  or a  $^5\text{B}_{1g}$  ground state.<sup>66,68</sup> It was demonstrated in refs 68 and 69 that (i) a  $^5\text{A}_{1g}$  ground state is obtained for a trigonal bipyramidal (5 coordinate) or a tetragonally compressed octahedral (6 coordinate) ligand geometry with a vacant electron  $d_{z^2}$  orbital. Spectroscopically this manifests itself as both a positive fine structure parameter ( $d(\text{Mn}^{\text{III}})$ ) and yields a negative hyperfine tensor anisotropy ( $\Delta a_{\text{aniso}} = a_{\parallel} - a_{\perp}$ , see above); (ii) a  $^5\text{B}_{1g}$  ground state is obtained for a square-pyramidal (5 coordinate) or tetragonally elongated (6 coordinate) ligand geometry. In this case the vacant electron orbital is now the  $d_{x^2 - y^2}$  orbital. Spectroscopically this manifests itself as both a negative fine structure parameter ( $d(\text{Mn}^{\text{III}})$ ) and yields a positive hyperfine tensor anisotropy. This behavior was observed for monomeric  $\text{Mn}^{\text{III}}$  model complexes and mixed valence  $\text{Mn}^{\text{II}}\text{Mn}^{\text{III}}$  and  $\text{Mn}^{\text{III}}\text{Mn}^{\text{IV}}$  dimers. The only exception known is the complex *trans*- $[\text{Mn}(\text{cyclam})_2]\text{I}$ ,<sup>70</sup> which is thought to have unique, low-lying charge transfer states which strongly perturb the ground state multiplet. As the  $\text{Mn}^{\text{III}}$  ion of the **PivOH** complex displays a negative fine structure parameter ( $d(\text{Mn}^{\text{III}})$ ) and the anisotropy of its hyperfine tensor is positive, its ground state is expected to be  $^5\text{B}_{1g}$ . This is consistent with the X-ray crystal structure of the **PivOH** complex which demonstrates the  $\text{Mn}^{\text{III}}$  ion has a tetragonally elongated (6 coordinate) ligand field. Thus all onsite parameters calculated using the method described above are consistent with literature benchmarks.

The large anisotropy of the effective  $G$ -tensor noted in section 4.2.1 can be explained using the calculated anisotropic spin projections described above. It is again expected that the onsite  $g$ -anisotropy of the  $\text{Mn}^{\text{II}}$  ion is small and thus the fitted anisotropy is a consequence of the onsite  $g$ -anisotropy of the  $\text{Mn}^{\text{III}}$  ion. This anisotropy is enhanced in the coupled basis as the parallel and perpendicular spin projections are significantly different; that is to say the  $G$ -anisotropy is large because the exchange coupling between the two Mn ions is small. Again it is the onsite fine structure tensor of the  $\text{Mn}^{\text{III}}$  ion that maps into the effective  $G$ -tensor as described above for the  $\text{Mn}^{\text{II}}/\text{Mn}^{\text{III}}$  hyperfine tensors. The onsite  $g$ -anisotropy of the  $\text{Mn}^{\text{III}}$  ion must be such that the parallel component of the  $g$ -tensor ( $g_z$ ) is smaller than the equatorial components of the  $g$ -tensor ( $g_x, g_y$ ). This is consistent within the set of mixed valence Mn dimers ( $\text{Mn}^{\text{III}}\text{Mn}^{\text{IV}}$  and  $\text{Mn}^{\text{II}}\text{Mn}^{\text{III}}$ ). Note that the same  $g$ -anisotropy for the  $\text{Mn}^{\text{III}}$  ion in  $\text{Mn}^{\text{III}}\text{Mn}^{\text{IV}}$  complexes results in the opposite  $G$ -anisotropy as seen in  $\text{Mn}^{\text{II}}\text{Mn}^{\text{III}}$  complexes since in the former the  $\text{Mn}^{\text{III}}$  carries the larger (positive) spin projection as opposed to the latter where it carries the smaller (negative) spin projection.

**4.3. DFT.** Calculations of EPR parameters using DFT were performed to further refine and support the analysis of the

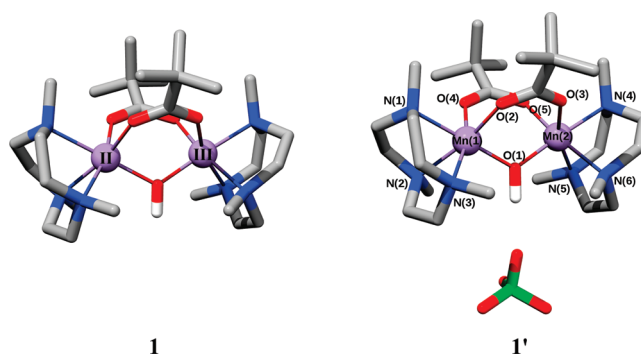


**Figure 5.** Geometries for models **1** and **1'** based on XRD crystal structure coordinates. All but the bridging hydroxo hydrogen atoms are omitted for clarity. Mn, C, N, O, H, Cl are colored purple, gray, blue, red, white, and green, respectively.

experimental EPR data. The calculated values, including the tensor orientations, are consistent with the presented interpretation of the experimentally recorded EPR spectra. The implications of the calculated results on future computational studies of more complex but related systems, such as the OEC, are discussed.

**4.3.1. Model Complex Geometries.** Six models were considered in the calculations. Models **1**, **1'**, **2**, **2'**, **3**, and **3'** were generated from the X-ray crystal structure published previously.<sup>20</sup> Model **1** was constrained to the previously determined X-ray crystal structure coordinates<sup>20</sup> while optimizing the positions of the hydrogen atoms. Model **2** represents the high-spin geometry optimization ( $S = 9/2$ ) while model **3** represents the optimized geometry obtained using the broken-symmetry formalism with an effective spin of  $S_T = 1/2$ . Additional models (**1'**, **2'**, and **3'**), which include the  $\text{ClO}_4^-$  counterion located near the bridging  $\mu\text{-OH}$  seen in the X-ray crystal structure were also examined and optimized in exactly the same way. Figure 5 shows the geometries for models **1** and **1'** and the oxidation states for each Mn.

In the Supporting Information S4 selected geometric parameters for each model of the **PivOH** complex are given. The crystal structure (models **1** and **1'**) contains two well separated Mn transition metal centers with a largely uniform octahedral ligand environment around the  $\text{Mn}^{\text{II}}$  ion and a  $\text{Mn}^{\text{III}}$  ion in a tetragonally elongated octahedral ligand field, with the Jahn–Teller axis located along the  $\text{Mn}^{\text{III}}\text{--N}(5)$  bond (see Figure 5). The optimized geometries of the **PivOH** complex (models **3** and **3'**) using the broken-symmetry approach lead to similar geometric features with shorter Mn–Mn distances and longer, on average, Mn–N bond lengths. Significantly, the broken-symmetry optimized geometry without the counterion, **3**, shows an out of plane bend of the hydrogen on the  $\mu\text{-OH}$  bridge with respect to the plane formed by the two Mn ions and the oxygen atom of the bridge, see the Supporting Information S4. This is inconsistent with the other models where the proton of the  $\mu\text{-OH}$  bridge is coplanar with the Mn ions and the oxygen atom of the bridge, as depicted in Figure 5. It should be noted that the geometries optimized in the high-spin state, the current preferred methodology for Mn dimers<sup>47,48</sup> have symmetric Mn centers, indicating a delocalization of the unpaired electrons between the two transition metal centers. This interpretation is further supported by an analysis of the calculated Mulliken spin populations, presented in Supporting Information S5. In the high-spin state,  $S = 9/2$ , model geometries **1**, **1'**, **3**, and **3'** show well-defined spin populations near 5.0 and 4.0 for the  $\text{Mn}^{\text{II}}$  and  $\text{Mn}^{\text{III}}$ , respectively. For the models **2** and **2'**, optimized in the high-spin

Table 2. Calculated Intrinsic  $^{55}\text{Mn}$  Hyperfine Coupling Constants (MHz)<sup>a</sup>

	onsite $^{55}\text{Mn}$ hyperfine tensors (MHz)										
	$\text{Mn}^{\text{II}}$					$\text{Mn}^{\text{III}}$					rmsd
	$a_x$	$a_y$	$a_z$	$a_{\text{iso}}$	$a_{\text{aniso}}$	$a_x$	$a_y$	$a_z$	$a_{\text{iso}}$	$a_{\text{aniso}}$	
1	-226.8	-225.7	-234.1	-228.9	-7.8	-273.9	-234.3	-127.2	-211.8	126.9	12.2
1'	-227.5	-226.7	-234.2	-229.5	-7.1	-280.1	-227.0	-129.3	-212.1	124.2	9.2
2	-219.2	-216.0	-228.9	-221.4	-11.2	-262.7	-254.3	-121.0	-212.7	137.5	23.1
2'	-212.8	-211.1	-227.4	-217.1	-15.4	-284.7	-218.1	-117.5	-206.8	133.9	18.4
3	-228.7	-228.2	-234.2	-230.4	-5.7	-261.9	-221.0	-119.0	-200.6	122.4	14.1
3'	-227.2	-225.8	-232.9	-228.7	-6.4	-260.8	-208.4	-110.1	-193.1	124.5	17.5
exp.	-239.7	-238.8	-240.0	-239.5	-0.7	-286.6	-218.1	-136.6	-213.8	115.8	

<sup>a</sup>Calculated values scaled by a factor of 1.50, see the Supporting Information S8. The  $a$  values are the average of the individual value:  $a_{\text{iso}} = (a_x + a_y + a_z)/3$ . The perpendicular and parallel  $a$  values are defined as:  $a_{\perp} = (a_x + a_y)/2$ ,  $a_{\parallel} = a_z$ . The anisotropy of  $a_i$  is expressed as the difference between the parallel and perpendicular component of the tensor. Calculated tensor components were re-oriented to the experimental.

state, each Mn center shows a spin population of approximately 4.5 indicating a delocalization of electron spin between the two metal centers. Application of the broken symmetry approach leads to a localization of spin of approximately 5.0 and -4.0 for the  $\text{Mn}^{\text{II}}$  and  $\text{Mn}^{\text{III}}$ , respectively.

**4.3.2. Heisenberg Exchange Coupling Constants.** The exchange coupling constant for the **PivOH** complex has been determined experimentally to be antiferromagnetic and small, on the order of  $-10 \text{ cm}^{-1}$ . In our previous BS-DFT study of Mn dimers, exchange coupling constants calculated using the single geometry approach described in Theory section 3.5 gave a variation between experiment and theory of  $27.1 \text{ cm}^{-1}$  (rmsd), see Orio et al.,<sup>48</sup> three times greater than the experimental exchange coupling for **PivOH**. Given the relatively large error found in this previous study the extent to which the single geometry approach can produce reliable estimates for exchange constant ( $J$ ) for the **PivOH** complex is marginal at best.

Calculated "single geometry" exchange coupling constants for each model complex are given in the Supporting Information S6. Models 1, 1', 2, and 2' indicate ferromagnetic behavior for the **PivOH** complex, contrary to experiment. Models 2 and 2' have strongly ferromagnetic calculated values near  $140 \text{ cm}^{-1}$ , indicative of spin delocalization as discussed above. Only models 3 and 3' show the correct antiferromagnetic behavior. For these models, 3 and 3', the calculated couplings deviate from the experimental value determined from EPR measurements by  $9.65 \text{ cm}^{-1}$  and  $4.47 \text{ cm}^{-1}$  respectively, both of which can be considered well within the expected error seen in the previous study.<sup>48</sup> The better estimation for the exchange coupling in model 3' over 3 can be attributed to the presence of the  $\text{ClO}_4^-$  counterion. As stated above, model 3, without the counterion, shows an out of plane bend of the  $\mu\text{-OH}$  bridge proton with respect to the plane formed by the two Mn ions and the bridging oxygen atom (see the Supporting Information S4). The effect of this subtle change in geometry, which presumably describes some change in the superexchange pathway between the two Mn ions, leads to an increase in the energy gap between the calculated high-spin and the broken-symmetry states giving a larger calculated antiferromagnetic coupling for model 3 than for model 3'.

The methodology for the calculation of exchange coupling constants as described by Orio et al.<sup>48</sup> can be improved by using the adiabatic energy difference as seen for calculations on a

$\text{Mn}^{\text{III}}\text{Mn}^{\text{IV}}$  DTNE model complex and models of dimanganese catalase.<sup>47,71</sup> The calculated adiabatic exchange coupling constant, using eq 13 (see Theory section 3.5), includes respective terms from the high-spin and broken-symmetry geometries. From a theoretical perspective this treatment for calculating the exchange coupling constants is preferred, as the experiments are adiabatic in nature. For a more complete discussion of the adiabatic approach see ref 40. For the models presented here, extremely good agreement, with an error of  $4.9 \text{ cm}^{-1}$ , is achieved between theory and experiment using the adiabatic energy difference for models 2' and 3'. A further improvement in the calculated exchange coupling constant can be made through the application of a van der Waals (VDW) correction,<sup>33</sup> accounting for weak interactions within each model structure which are different for the high-spin and broken symmetry geometries. For exchange coupling constants using a "single geometry" approach the VDW DFT dispersion correction does not contribute because of cancelation, see eq 13. This is because the VDW correction gives an energy correction related to the geometry and density functional used, but is not related to the spin state of the system being studied. As such both the high-spin and broken symmetry states for a single geometry have the same correction applied. Using both the adiabatic approximation and the VDW correction, the adiabatic energy difference for models 2' and 3' gives an error of only  $2.6 \text{ cm}^{-1}$ . However, similar agreement is lacking for the calculated exchange using models 2 and 3. Again, this is due to the aforementioned out of plane bend of the  $\mu\text{-OH}$  bridge proton which leads to a significant stabilization of the broken-symmetry geometry over that of the high-spin geometry.

**4.3.3.  $^{55}\text{Mn}$  Hyperfine Tensors.** The calculated intrinsic site  $^{55}\text{Mn}$  hyperfine values are shown in Table 2 as compared to the experimental determination discussed above. Comparison of intrinsic site values was chosen over the more conventional spin projected comparison, because of the largely anisotropic spin projection tensors determined from the analysis of the on-site fine structure parameter of the  $\text{Mn}^{\text{III}}$ . Within the framework of BS-DFT it is currently not possible to account for the on-site fine structure parameters of individual ions in complexes of effective ground state spins of  $S_T = 1/2$ , such as **PivOH**. However, as is shown in Table 2 the intrinsic site hyperfine couplings for transition metal ions within such systems can be calculated to a high degree of accuracy. Excellent agreement (within 5%) is seen between the experimental values reported in section 4.2.4

**Table 3.** Calculated  $^{55}\text{Mn}$  Nuclear Quadrupole Coupling Constants<sup>a</sup>

	nuclear quadrupole couplings ( $p_i$ )			
	$\text{Mn}^{\text{II}}$		$\text{Mn}^{\text{III}}$	
	$p$	$\eta$	$p$	$\eta$
1	-1.83	0.661	2.49	0.838
1'	-0.74	0.783	-3.52	0.262
2	-1.84	0.446	2.18	0.787
2'	-0.76	0.749	-2.72	0.614
3	-1.86	0.614	2.14	0.908
3'	-0.72	0.460	-2.23	0.439
exp.	-1.62	0.73	-2.00	0.38

<sup>a</sup>The nuclear quadrupole coupling constant  $p$  is defined as:  $p = (e^2qQ)/(4hI(2I - 1)) = (p_3/2)$  and  $\eta = (p_1 - p_2)/(p_3)$ .  $p_1$ ,  $p_2$ , and  $p_3$  are defined such that  $|p_1| \leq |p_2| < |p_3|$ .

(Table 1) and the calculations presented here. It is noted that a comparison of experimental (the fitted or effective Spin Hamiltonian parameters) and the projected DFT values, using the standard method of scalar, isotropic spin-projections still yields a reasonably good agreement (within 10%) of the experimentally determined  $A_{\text{iso}}$  values; however, the agreement of the calculated anisotropy is, as expected, much poorer.

As has been discussed earlier, the anisotropy of the Mn transition metal centers in the coupled basis is inverted from the anticipated solution, that is, that of a largely isotropic  $\text{Mn}^{\text{II}}$  and an anisotropic  $\text{Mn}^{\text{III}}$ . In section 4.2.4, this was explained by the inclusion of the fine structure tensor of the  $\text{Mn}^{\text{III}}$  ion. It was shown that if this term is included, the intrinsic hyperfine parameters for both Mn ions match expectations derived from monomer studies. The DFT calculations presented here support this analysis (Table 2 and Supporting Information S9). The calculated intrinsic site values reproduce the tensor anisotropies seen for the experiment, namely, an isotropic  $\text{Mn}^{\text{II}}$  ( $a_{\text{aniso}} < 10$  MHz) and a highly anisotropic  $\text{Mn}^{\text{III}}$  ion ( $a_{\text{aniso}} \sim 100$  MHz) and thus support the notion that the projected anisotropies of the Mn centers cannot be explained without the use of tensor spin-projections. The best agreement with experiment is given by model 1' with models 1, 3, and 3' giving slightly larger errors. The models optimized in the high spin state, 2 and 2', show larger anisotropies for the  $\text{Mn}^{\text{II}}$ , symptomatic of the symmetric geometry observed in these models. It should be noted that the high spin models, 2 and 2', still show remarkable agreement with experiment with maximal errors of 17% and 14% in the tensor components with respect to the experimentally determined values, respectively. Indeed errors for the isotropic component of the intrinsic site hyperfine tensors is less than 10% and as low as 0.5% for the high spin models, although this level of agreement is achieved through a convenient cancellation of errors. For more complete agreement between the calculated and experimentally determined values the models based on either the crystal structure geometry or the broken-symmetry optimized geometries are needed.

**4.3.4.  $^{55}\text{Mn}$  Nuclear Quadrupole Tensors.** The calculated nuclear quadrupole couplings for each  $^{55}\text{Mn}$  nucleus are shown in Table 3. The best agreement with experiment is found in models without the  $\text{ClO}_4^-$  counterion, although the electric field gradient of the  $\text{Mn}^{\text{III}}$  for all models is calculated as much too

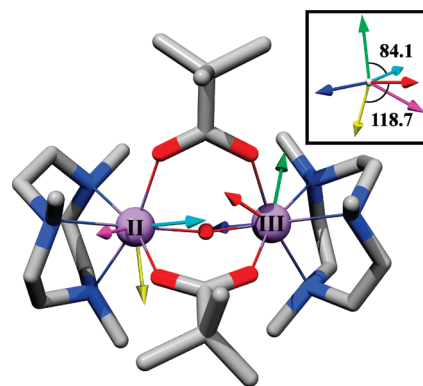


**Figure 6.** Relative orientation of calculated electric field gradient components in model 1 following the standard convention:  $|p_1| \leq |p_2| < |p_3|$ . Red, green, and blue arrows represent the orientation for  $p_1$ ,  $p_2$ , and  $p_3$  on  $\text{Mn}^{\text{III}}$ , respectively. Yellow, magenta, and cyan arrows represent the orientation for  $p_1$ ,  $p_2$ , and  $p_3$  on  $\text{Mn}^{\text{II}}$ . All other models without the  $\text{ClO}_4^-$  counterion show similar electric field gradient component orientations, see Supporting Information S10.

rhombic. In the presence of the counterion, model 1' gives good values with the exception of the magnitude of the  $\text{Mn}^{\text{II}}$  nuclear quadrupole coupling  $p(\text{Mn}^{\text{II}})$ , which is calculated as approximately 1 MHz too small. The significant differences seen between models 1 (2, 3), and 1' (2', 3') indicate the sensitivity of the calculated electric field gradient to the presence of the counterion even though it is more than 5 Å away from either Mn. A similar situation has previously been encountered for Fe complexes.<sup>72</sup> It is possible that the inclusion of additional counterions, seen in the crystal structure,<sup>20</sup> would improve the calculated results of the electric field gradient at the Mn.

The orientation of the quadrupole components were analyzed previously in the context of fitting the experimental spectrum. Figure 6 shows a representative depiction of the calculated relative orientations of the electric field gradient components for  $\text{Mn}^{\text{II}}$  and  $\text{Mn}^{\text{III}}$ . The calculated orientations for all three models broadly agree with the experimentally determined orientations, that is, through fitting of the experimental spectra, namely, that the components are roughly collinear but transposed (see also Supporting Information S10).

## DISCUSSION

**5.1. Comparison of EPR/ENDOR Data with BS-DFT Calculations.** The BS-DFT calculations presented above for the PivOH complex demonstrate the increasing utility of DFT theory with regard to spectral analysis of complicated exchange coupled systems. Here it is shown that even for a complex with a small exchange coupling, that is to say only a small energetic separation between the effective ground spin 1/2 state and the first excited state, robust estimates for all EPR observables can be made. In these systems though, care must be taken when comparing spectroscopic observables to onsite properties. Spectroscopic observables ( $^{55}\text{Mn}/^1\text{H}/^{14}\text{N}$ -hyperfine couplings) as deduced from the simulation of EPR/ENDOR data solved in the coupled basis represent effective values that must be correctly mapped to the uncoupled basis to yield the onsite values of the individual Mn ion. It is only then that these measurements provide meaningful results; they provide a window into the coordination sphere of Mn ions and their individual electronic

structure. The mapping requires a complete understanding of the zero-field splitting of the complex including the onsite contribution of each Mn. For this complex, which contains an isotropic spin center ( $\text{Mn}^{\text{II}}$ ), this can be achieved.

As demonstrated above, the appropriately mapped experimental EPR/ENDOR data and the onsite properties as estimated from DFT essentially match. All  $^{55}\text{Mn}$  hyperfine tensor components agree to within 10%. Thus, the EPR/ENDOR analysis, DFT calculations, and crystallographic data all arrive at the same result. All three correctly assign the nature of the  $\text{Mn}^{\text{III}}$  ion, its ground electronic state, and its coordination sphere and in doing so have the potential to accurately predict the chemistry the complex can perform.

**5.2. Implications for Further BS-DFT Studies on Mn Systems.** Current techniques for the calculation of  $^{55}\text{Mn}$  EPR parameters using BS-DFT focus largely on the calculation of the high-spin geometry. Importantly, it has been shown that for  $\text{Mn}^{\text{III}}$  and  $\text{Mn}^{\text{IV}}$  ions and related dimeric complexes, the calculated high-spin geometry yields a good representation of the real geometry of the complex as assessed by comparison to crystallographic data. The same is not seen here for the **PivOH** complex, a weakly coupled Mn-dimer which contains a  $\text{Mn}^{\text{II}}$  ion. The calculated high-spin geometry is significantly different from that of the crystal structure. The high spin geometry contains a unique electron delocalization and a bias toward ferromagnetic coupling, in contrast to all existing data seen in mixed valence Mn complexes studied so far. As such, particular care should be taken when applying BS-DFT methods to weakly coupled systems and those that contain low Mn oxidation states for the calculation of EPR parameters.

The inclusion of the  $\text{ClO}_4^-$  counterion had a non-negligible impact on the calculated EPR parameters presented in this work. Specifically the calculated electric field gradient of both Mn ions was remarkably sensitive to this distant counterion ( $\sim 5 \text{ \AA}$ ). This observation is of importance for studies on metal cofactors in proteins. DFT models of these metal sites must be constructed in such a way that the influence of remote ions is considered, including counterions such as calcium or chloride and charged amino acid residues such as arginine or lysine. Without the inclusion of these charged groups, DFT estimates of charge sensitive properties, such as the nuclear quadrupole coupling constants, are limited.

**5.3. Implications for Current Studies of the OEC.** The combined experimental (EPR/ENDOR) and theoretical analysis (DFT) presented above validates a recent study performed in our laboratory on the tetramanganese ( $\text{Mn}^{\text{III}}\text{Mn}^{\text{IV}}_3$ ) cluster that comprises the OEC. In our earlier work we investigated the effect of the replacement of the  $\text{Ca}^{2+}$  ion with  $\text{Sr}^{2+}$ .<sup>73</sup>  $\text{Ca}^{2+}$  is an essential cofactor of the OEC that is structurally coupled to the Mn ions via  $\mu$ -oxo or  $\mu$ -hydroxo bridges. It was shown that this replacement does not significantly alter the overall electronic structure of the OEC. The changes that were observed were interpreted as evidence of a small modification of the fine structure tensor of the only  $\text{Mn}^{\text{III}}$  ion and was deduced using the same procedure as described here. It was further suggested that the sign of the fine structure parameters  $d$  of the  $\text{Mn}^{\text{III}}$  ion ( $d(\text{Mn}^{\text{III}})$ ) must be negative to reproduce the fitted Spin Hamiltonian parameters, which requires the  $\text{Mn}^{\text{III}}$  ion to have a 5 coordinate square-bipyramidal or 6 coordinate tetragonally elongated ligand field. This result is of importance as it potentially identifies one of the sites of substrate water binding. The only DFT structural model of the OEC in the current literature

consistent with the  $\text{Ca}^{2+}$  replacement study described above is the Siegbahn model.<sup>74</sup> As in models proposed by EXAFS spectroscopy<sup>75</sup> it contains three short Mn–Mn distances, and one long (3.3 Å) Mn–Mn distance. The long Mn–Mn distance is inside a distorted cuboidal structure and forms its open site. The missing “corner oxygen” leads to a 5 coordinate square-pyramidal ligation for the  $\text{Mn}^{\text{DIII}}$  ion in the  $S_2$  state. It is to this open coordination site that one of the substrate “waters” ( $\text{H}_2\text{O}$ ,  $\text{OH}^-$ ) could bind during the  $S_2 \rightarrow S_3$  transition (either from bulk water, or water bound to  $\text{Ca}^{2+}$ ). The 3.3 Å Mn–Mn distance within the distorted cuboid could then provide an ideal geometry for low energy barrier O–O bond formation during the  $S_3 \rightarrow S_4 \rightarrow S_0$  transition.<sup>74,76–78</sup>

The results and analyses presented here are equally applicable to the lower oxidation states of the OEC including the  $S_0$  and  $S_{-2}$  states.  $S_0$ , the lowest oxidation state obtained by the OEC during the catalytic cycle, most probably contains three  $\text{Mn}^{\text{III}}$  ions and one  $\text{Mn}^{\text{IV}}$  (see refs 13,79). The  $S_{-2}$  state is instead a reduced form of the OEC. It is generated by the addition of exogenous chemical reductants such as  $\text{NH}_2\text{OH}$ ,  $\text{NH}_2\text{NH}_2$ , or  $\text{NO}$ .<sup>80–83</sup> It is thought that this state may represent an assembly intermediate with net oxidation state  $(\text{Mn}^{\text{III}})_3\text{Mn}^{\text{II}}$ .<sup>84,85</sup> These states both represent weakly antiferromagnetically coupled systems where an intrinsically isotropic spin ( $\text{Mn}^{\text{II}}$ , octahedral  $\text{Mn}^{\text{IV}}$ ) is coupled to an intrinsically anisotropic spin ( $\text{Mn}^{\text{III}}$ ), the same situation seen for the **PivOH** complex.

## 6. CONCLUSIONS

The  $\text{Mn}^{\text{II}}\text{Mn}^{\text{III}}$  **PivOH** and related dimeric complexes represent robust structural mimics of several metal cofactors of biological enzymes. The relevance of the **PivOH** complex for the OEC of Photosystem II was discussed above, but a comparison can be equally made for (i) the dimanganese catalase,<sup>1,2</sup> which catalyzes the dismutation of  $\text{H}_2\text{O}_2$  to  $\text{H}_2\text{O}$  and  $\text{O}_2$ ; or (ii) the recently identified Mn containing class Ib/Ic ribonucleotide reductases,<sup>3,4,86–88</sup> to name but two examples. The experimental and theoretical methodologies developed for the **PivOH** complex described above should be directly applicable to these biological systems. Similarly, this model provides important empirical benchmarks for all spectroscopic observables.

The EPR/ENDOR measurements and DFT calculations presented here serve as a demonstration that these methods, when used in tandem can provide a complete picture of the electronic structure of highly complicated metal systems. In the circumstance where X-ray crystallography is unattainable or at very least compromised, the combined EPR/ENDOR and DFT approach described here is the obvious recourse as it essentially provides complementary information. This is of particular relevance to metal cofactors in proteins, which cannot often be measured using crystallographic techniques, especially when poised in catalytically relevant higher oxidation states.

Future studies on manganese containing enzymes such as these systems require a shift in scope. From the results presented here, BS-DFT can provide reliable estimates for nearly all magnetic spectroscopic parameters when appropriately optimized for the system of interest. This includes the hyperfine tensor anisotropy, which is often disregarded in the discussion of BS-DFT results. It is this feature that will provide important information with regard to the ligand geometry of metal ions of multicenter active sites and the subsequent elucidation of their reaction mechanisms.

## ■ ASSOCIATED CONTENT

**S Supporting Information.** Additional material detailing (1) magnetic susceptibility data and error plots; (2) derivation of Mn<sup>III</sup> fine structure constant from 1st-order perturbation theory; (3) fitting of EPR/ENDOR spectra using noncollinear tensors; (4) geometric parameters for model complexes; (5) manganese Mulliken spin populations; (6) BS-DFT calculated exchange coupling constants; (7) basis sets used for EPR parameter calculations; (8) determination of the <sup>55</sup>Mn hyperfine scaling factor for use with broken-symmetry DFT; (9) calculated <sup>55</sup>Mn hyperfine orientations; (10) calculated <sup>55</sup>Mn quadrupole/electric field gradient orientations; (11) sample input files for DFT calculations. This material is available free of charge via the Internet at <http://pubs.acs.org>.

## ■ AUTHOR INFORMATION

### Corresponding Author

\*Phone: +49-208-306-3552 (N.C.), +49-208-306-3614 (W.L.).  
E-mail: [cox@mpi-muelheim.mpg.de](mailto:cox@mpi-muelheim.mpg.de) (N.C.), [wolfgang.lubitz@mpi-mail.mpg.de](mailto:wolfgang.lubitz@mpi-mail.mpg.de) (W.L.).

## ■ ACKNOWLEDGMENT

The authors acknowledge Dr. T. Weyhermüller and Dr. E. Bill for their assistance with the collection of experimental data and its interpretation and their help in the preparation of the manuscript. Financial support was provided by the DFG (Me1629/2-4), the Max Planck Society, the EU SOLAR-H2 (FP7 contract 212508), and the Wallenberg and Kempe foundations (J.M.). L.R. is a fellow of the North Rhine-Westphalia (NRW) Research School BioStruct program.

## ■ REFERENCES

- Barynin, V. V.; Whittaker, M. M.; Antonyuk, S. V.; Lamzin, S. V.; Harrison, P. M.; Artymiuk, A. J.; Whittaker, J. M. *Structure* **2001**, *9*, 725–738.
- Dismukes, G. C. *Chem. Rev.* **1996**, *96*, 2909–2926.
- Cox, N.; Ogata, H.; Stolle, P.; Reijerse, E.; Auling, G.; Lubitz, W. *J. Am. Chem. Soc.* **2010**, *132*, 11197–11213.
- Cotruvo, J. A.; Stubbe, J. *Biochemistry* **2010**, *49*, 1297–1309.
- Teutloff, C.; Schäfer, K.-O.; Sinnecker, S.; Barynin, V.; Bittl, R.; Wieghardt, K.; Lendzian, F.; Lubitz, W. *Magn. Reson. Chem.* **2005**, *43*, S51–S64.
- Schäfer, K. O.; Bittl, R.; Lendzian, F.; Barynin, V. V.; Weyhermüller, T.; Wieghardt, K.; Lubitz, W. *J. Phys. Chem. B* **2003**, *107*, 1242–1250.
- Schweiger, A.; Jeschke, G. *Principles of Pulsed Electron Paramagnetic Resonance*; Oxford University Press: Oxford, 2001.
- Kulik, L. V.; Lubitz, W. *Photosynth. Res.* **2009**, *102*, 391–401.
- Randall, D. W.; Sturgeon, B. E.; Ball, J. A.; Lorigan, G. A.; Chan, M. K.; Klein, M. P.; Armstrong, W. H.; Britt, R. D. *J. Am. Chem. Soc.* **1995**, *117*, 11780–11789.
- Randall, D. W.; Chan, M. K.; Armstrong, W. H.; Britt, R. D. *Mol. Phys.* **1998**, *95*, 1283–1294.
- Peloquin, J. M.; Campbell, K. A.; Randall, D. W.; Evanchik, M. A.; Pecoraro, V. L.; Armstrong, W. H.; Britt, R. D. *J. Am. Chem. Soc.* **2000**, *122*, 10926–10942.
- Kulik, L.; Epel, B.; Messinger, J.; Lubitz, W. *Photosynth. Res.* **2005**, *84*, 347–353.
- Kulik, L. V.; Epel, B.; Lubitz, W.; Messinger, J. *J. Am. Chem. Soc.* **2007**, *129*, 13421–13435.
- Zweygart, W.; Bittl, R.; Wieghardt, K.; Lubitz, W. *Chem. Phys. Lett.* **1996**, *261*, 272–276.
- Kulik, L. V.; Lubitz, W.; Messinger, J. *Biochemistry* **2005**, *44*, 9368–9374.
- Larson, E.; Haddy, A.; Kirk, M. L.; Sands, R. H.; Hatfield, W. E.; Pecoraro, V. L. *J. Am. Chem. Soc.* **1992**, *114*, 6263–6265.
- Diril, H.; Chang, H. R.; Zhang, X.; Larsen, S. K.; Potenza, J. A.; Pierpont, C. G.; Schugar, H. J.; Isied, S. S.; Hendrickson, D. N. *J. Am. Chem. Soc.* **1987**, *109*, 6207–6208.
- Chang, H. R.; Larsen, S. K.; Boyd, P. D. W.; Pierpont, C. G.; Hendrickson, D. N. *J. Am. Chem. Soc.* **1988**, *110*, 4565–4576.
- Zheng, M.; Khangulov, S. V.; Dismukes, G. C.; Barynin, V. V. *Inorg. Chem.* **1994**, *33*, 382–387.
- Bossek, U.; Hummel, H.; Weyhermüller, T.; Wieghardt, K.; Russell, S.; van der Wolf, L.; Kolb, U. *Angew. Chem.* **1996**, *108*, 1653–1656.
- Using the  $H = -2J_{S_1} \cdot S_2$  as opposed to  $H = -J_{S_1} \cdot S_2$  convention.
- O'Connor, C. J. *Prog. Inorg. Chem.* **1982**, *29*, 203–283.
- Weast, R. C.; Astle, M. J. *CRC Handbook of Chemistry and Physics*; CRC Press Inc.: Boca Raton, FL, 1979.
- Bill, E. *JulX*, version 1.41; Max-Planck-Institut: Muelheim an der Ruhr, Germany, 2008; [http://ewww.mpi-muelheim.mpg.de/bac/logins/bill/julX\\_en.php](http://ewww.mpi-muelheim.mpg.de/bac/logins/bill/julX_en.php).
- Lebedev, V. I.; Laikov, D. N. *Doklady Math.* **1999**, *59*, 477.
- Wang 2003, <http://server.ccl.net/ccca/software/SOURCES/>
- Epel, B.; Gromov, I.; Stoll, S.; Schweiger, A.; Goldfarb, D. *Concepts Magn. Res. B* **2005**, *26B*, 36–45.
- Kulik, L. V.; Epel, B.; Lubitz, W.; Messinger, J. *J. Am. Chem. Soc.* **2005**, *127*, 2392–2393.
- Epel, B.; Arieli, D.; Baute, D.; Goldfarb, D. *J. Magn. Reson.* **2003**, *164*, 78–83.
- Stoll, S.; Schweiger, A. *J. Magn. Reson.* **2006**, *178*, 42–55.
- Becke, A. D. *Phys. Rev. A* **1988**, *38*, 3098–3100.
- Perdew, J. P. *Phys. Rev. B* **1986**, *33*, 8822–8824.
- Grimme, S.; Antony, J.; Ehrlich, S.; Krieg, H. *J. Chem. Phys.* **2010**, *132*, 154104.
- van Wüllen, C. *J. Chem. Phys.* **1998**, *109*, 392–399.
- van Lenthe, E.; Baerends, E. J.; Snijders, J. G. *J. Chem. Phys.* **1993**, *99*, 4597–4610.
- van Lenthe, E.; Ehlers, A.; Baerends, E.-J. *J. Chem. Phys.* **1999**, *110*, 8943–8953.
- Pantazis, D. A.; Chen, X. Y.; Landis, C. R.; Neese, F. *J. Chem. Theory Comput.* **2008**, *4*, 908–919.
- Weigend, F. *Phys. Chem. Chem. Phys.* **2006**, *8*, 1057–1065.
- Neese, F. *ORCA—an ab initio, Density Functional and Semiempirical Program Package*, v. 2.6-35; University of Bonn: Bonn, Germany, 2007.
- Neese, F. *Coord. Chem. Rev.* **2009**, *253*, 526–563.
- Noodleman, L. *J. Chem. Phys.* **1981**, *74*, 5737–5743.
- Noodleman, L.; Case, D. A. *Adv. Inorg. Chem.* **1992**, *38*, 423–470.
- Noodleman, L.; Davidson, E. R. *Chem. Phys.* **1986**, *109*, 131–143.
- Staroverov, V. N.; Scuseria, G. E.; Tao, J.; Perdew, J. P. *J. Chem. Phys.* **2003**, *119*, 12129–12137.
- Neese, F.; Wennmohs, F.; Hansen, A.; Becker, U. *Chem. Phys.* **2009**, *356*, 98–109.
- Neese, F. *Inorg. Chim. Acta* **2002**, *337*, 181–192.
- Sinnecker, S.; Neese, F.; Noodleman, L.; Lubitz, W. *J. Am. Chem. Soc.* **2004**, *126*, 2613–2622.
- Orio, M.; Pantazis, D. A.; Petrenko, T.; Neese, F. *Inorg. Chem.* **2009**, *48*, 7251–7260.
- Pantazis, D. A.; Krewald, V.; Orio, M.; Neese, F. *Dalton Trans.* **2010**, *39*, 4959–4967.
- Baffert, C.; Orio, M.; Pantazis, D. A.; Duboc, C.; Blackman, A. G.; Blondin, G.; Neese, F.; Deronzier, A.; Collomb, M.-N. *Inorg. Chem.* **2009**, *48*, 10281–10288.
- Pantazis, D. A.; Orio, M.; Petrenko, T.; Zein, S.; Bill, E.; Lubitz, W.; Messinger, J.; Neese, F. *Chem.—Eur. J.* **2009**, *15*, 5108–5123.

- (52) Pantazis, D. A.; Orio, M.; Petrenko, T.; Zein, S.; Lubitz, W.; Messinger, J.; Neese, F. *Phys. Chem. Chem. Phys.* **2009**, *11*, 6788–6798.
- (53) Sage, J. T.; Xia, Y. M.; Debrunner, P. G.; Keough, D. T.; de Jersey, J.; Zerner, B. *J. Am. Chem. Soc.* **1989**, *111*, 7239–7247.
- (54) Bencini, A.; Gatteschi, D. *EPR of Exchange Coupled Systems*; Springer-Verlag: Berlin, Germany, 1990.
- (55) Yamaguchi, K.; Takahara, Y.; Fueno, T. *Applied Quantum Chemistry*; Springer: New York, 1986; p 155.
- (56) Yamanaka, S.; Kawakami, T.; Nagao, H.; Yamaguchi, K. *Chem. Phys. Lett.* **1994**, *231*, 25–33.
- (57) Schäfer, K. O. Exchange Coupled Manganese Complexes: Model Systems for the Active Centres of Redoxproteins Investigated with EPR Techniques. Doctoral Thesis, Technische Universität, Berlin, Germany, 2002.
- (58) Schweiger, A.; Jeschke, G. *Principles of pulse electron paramagnetic resonance*, Oxford University Press: Oxford, England, 2001; Vol. 1.
- (59) Monomeric Mn<sup>II</sup>, Mn<sup>III</sup>, and Mn<sup>IV</sup> complexes all have  $S > 1/2$ . As such, multiple sets of spectral lines are observed. For example Mn<sup>II</sup> exhibits spectral lines centered at  $a/2$ ,  $3a/2$ , and  $5a/2$ .
- (60) Schäfer, K. O.; Bittl, R.; Zweggart, W.; Lendzian, F.; Haselhorst, G.; Weyhermüller, T.; Wieghardt, K.; Lubitz, W. *J. Am. Chem. Soc.* **1998**, *120*, 13104–13120.
- (61) Abragam, A.; Bleaney, B. *Electron Paramagnetic Resonance of Transition Metal Ions*; Clarendon Press: Oxford, England, 1970.
- (62) Blanchard, S.; Rivière, G. B.; Nierlich, M.; Girerd, J.-J. *Inorg. Chem.* **2003**, *42*, 4568–4578.
- (63) Duboc, C.; Astier-Perret, V.; Chen, H.; Pécaut, J.; Crabtree, R. H.; Brudvig, G. W.; Collomb, M.-N. *Inorg. Chim. Acta* **2006**, *359*, 1541–1548.
- (64) Duboc, C.; Collomb, M.-N.; Pécaut, J.; Deronzier, A.; Neese, F. *Chem.—Eur. J.* **2008**, *14*, 6498–6509.
- (65) Duboc, C.; Phoeung, T.; Jouvenot, D.; Blackman, A. G.; McClintock, L. F.; Pécaut, J.; Collomb, M.-N.; Deronzier, A. *Polyhedron* **2007**, *26*, 5243–5249.
- (66) Griffith, J. S. *The theory of Transition-Metal Ions*; Cambridge University Press: London, England, 1971.
- (67) Carrington, A.; McLachlan, A. D. *Introduction to Magnetic Resonance*, 1st ed.; Harper and Row: New York, 1967.
- (68) Gerritsen, H. J.; Sabisky, E. S. *Phys. Rev.* **1963**, *132*, 1507–1512.
- (69) Campbell, K. A.; Force, D. A.; Nixon, P. J.; Dole, F.; Diner, B. A.; Britt, R. D. *J. Am. Chem. Soc.* **2000**, *122*, 3754–3761.
- (70) Mossin, S.; Weihe, H.; Barra, A.-L. *J. Am. Chem. Soc.* **2002**, *124*, 8764–8765.
- (71) Sinnecker, S.; Neese, F.; Lubitz, W. *J. Biol. Inorg. Chem.* **2005**, *10*, 231–238.
- (72) Ray, K.; Begum, A.; Weyhermüller, T.; Piligkos, S.; van Slageren, J.; Neese, F.; Wieghardt, K. *J. Am. Chem. Soc.* **2005**, *127*, 4403–4415.
- (73) Cox, N.; Rapatskiy, L.; Su, J.-H.; Pantazis, D. A.; Sugiura, M.; Kulik, L.; Dorlet, P.; Rutherford, A. W.; Neese, F.; Boussac, A.; Lubitz, W.; Messinger, J. *J. Am. Chem. Soc.* **2011**, *133*, 3635–3648.
- (74) Siegbahn, P. E. M. *Acc. Chem. Res.* **2009**, *42*, 1871–1880.
- (75) Yano, J.; Kern, J.; Sauer, K.; Latimer, M. J.; Pushkar, Y.; Biesiadka, J.; Loll, B.; Saenger, W.; Messinger, J.; Zouni, A.; Yachandra, V. K. *Science* **2006**, *314*, 821–825.
- (76) Messinger, J. *Phys. Chem. Chem. Phys.* **2004**, *6*, 4764–4771.
- (77) Zein, S.; Kulik, L. V.; Yano, J.; Kern, J.; Pushkar, Y.; Zouni, A.; Yachandra, V. K.; Lubitz, W.; Neese, F.; Messinger, J. *Phil. Trans. R. Soc.* **2008**, *363*, 1167–1177.
- (78) Petrie, S.; Stranger, R.; Pace, R. J. *Angew. Chem.* **2010**, *122*, 4329–4332.
- (79) Yachandra, V. K.; Sauer, K.; Klein, M. P. *Chem. Rev.* **1996**, *96*, 2927–2950.
- (80) Messinger, J.; Renger, G. *FEBS Lett.* **1990**, *277*, 141–146.
- (81) Hanley, J.; Sarrou, J.; Petrouleas, V. *Biochemistry* **2000**, *39*, 15441–15445.
- (82) Ioannidis, N.; Sarrou, J.; Schansker, G.; Petrouleas, V. *Biochemistry* **1998**, *37*, 16445–16451.
- (83) Sarrou, J.; Isgandarova, S.; Kern, J.; Zouni, A.; Renger, G.; Lubitz, W.; Messinger, J. *Biochemistry* **2003**, *42*, 1016–1023.
- (84) Tamura, N.; Cheniae, G. *Biochim. Biophys. Acta* **1987**, *890*, 179–194.
- (85) Ono, T. *Biochim. Biophys. Acta* **2001**, *1503*, 40–51.
- (86) Jiang, W.; Yun, D.; Saleh, L.; Barr, E. W.; Xing, G.; Hoffart, L. M.; Maslak, M.-A.; Krebs, C.; Bollinger, J. M. *Science* **2007**, *316*, 1188–1191.
- (87) Jiang, W.; Yun, D.; Saleh, L.; Bollinger, J. M.; Krebs, C. *Biochemistry* **2008**, *47*, 13736–13744.
- (88) Voevodskaya, N.; Lendzian, F.; Ehrenberg, A.; Gräslund, A. *FEBS Lett.* **2007**, *581*, 3351–3355.